Non-Equilibrium Lattice Dynamics in Photo-Excited Two-Dimensional Perovskites

Shelby A Cuthriell, Shobhana Panuganti, Craig C Laing, Michael A Quintero, Burak Guzelturk, Nuri Yazdani, Boubacar Traore, Alexandra Brumberg, Christos D Malliakas, Aaron M Lindenberg, et al.

Advanced Materials https://doi.org/10.1002/adma.202202709

https://onlinelibrary.wiley.com/doi/10.1002/adma.202202709

Non-Equilibrium Lattice Dynamics in Photo-Excited Two-Dimensional Perovskites

Shelby A. Cuthriell[1], Shobhana Panuganti[1], Craig C. Laing[1], Michael A. Quintero[1], Burak Guzelturk[2], Nuri Yazdani[3,4], Boubacar Traore[5], Alexandra Brumberg[1], Christos D. Malliakas[1], Aaron M. Lindenberg[3,7], Vanessa Wood[4], Claudine Katan[5], Jacky Even[6], Xiaoyi Zhang[2], Mercouri G. Kanatzidis[1*], Richard D. Schaller[1,8*]

[1]Department of Chemistry, Northwestern University, 2145 N. Sheridan Road, Evanston, Illinois 60208, United States

[2]X-ray Science Division, Argonne National Laboratory, Lemont, Illinois 60439, United States

[3]Stanford Institute for Materials and Energy Sciences, SLAC National Accelerator Laboratory, Menlo Park, CA, USA.

[4]Department of Information Technology and Electrical Engineering, ETH Zurich, Zurich, Switzerland

[5]Univ Rennes, ENSCR, INSA Rennes, CNRS, ISCR (Institut des Sciences Chimiques de Rennes) - UMR 6226, Rennes F-35000, France

[6]Univ Rennes, INSA Rennes, CNRS, Institut FOTON - UMR 6082, Rennes F-35000, France

[7]Department of Materials Science and Engineering, Stanford University, Stanford, CA, USA.

[8]Center for Nanoscale Materials, Argonne National Laboratory, Lemont, Illinois 60439, United States

Corresponding authors: schaller@anl.gov, schaller@northwestern.edu, m-kanatzidis@northwestern.edu

Keywords

lead halide perovskite, two-dimensional, transient structure, optical excitation

https://onlinelibrary.wiley.com/doi/10.1002/adma.202202709

Abstract

The interplay between structural and photophysical properties of metal halide perovskites is critical to their utility in optoelectronic devices, but quantitative understanding of lattice response upon excitation is limited. Here, we investigate two-dimensional (2D) perovskites butylammonium lead iodide, $(BA)_2PbI_4$, and phenethylammonium lead iodide, $(PEA)_2PbI_4$, using ultrafast transient X-ray diffraction (TrXRD) as a function of optical excitation fluence to discern photoinduced structural dynamics. We find that both powder X-ray diffraction (PXRD) and time-resolved photoluminescence (TrPL) linewidths narrow over 1 ns following optical excitation for the fluence range studied, concurrent with slight red-shifting of the optical bandgaps. We attribute these observations to transient relaxation of distorted lead iodide octahedra stimulated mainly by electron-hole pair creation. The *c* axis expands up to 0.37% over hundreds of picoseconds; reflections sampling the *a* and *b* axes undergo one tenth of this expansion with the same timescale. Post-photo-excitation appearance of the (110) reflection in $(BA)_2PbI_4$ would suggest a transient phase transition; however, through new single crystal XRD we find reflections which violate glide plane conditions in the reported *Pbca* structure and reassign the static structure space group as $P2_12_12_1$; with this we rule out a non-equilibrium phase transition. These findings offer increased understanding of the appreciable lattice changes in 2D perovskites that occur upon electron-hole pair generation, and the resulting impacts on structural and electronic properties.

Introduction

Two-dimensional metal halide perovskites constitute an emerging class of solution-processable semiconductors that have drawn intense interest due to thickness- and composition-dependent electronic tunability, facile syntheses, and high defect tolerance, which make them attractive for use in a variety of optoelectronic applications.[1] These 2D variants form via self-assembly of organic ammonium cations and metal halide octahedra into quantum well structures. This dimensionality imparts quantum confinement of charge carriers and increases exciton binding energy due to reduced dielectric screening relative to the related 3D composition.[2] Population of low-frequency phonons and dynamic disorder at room temperature in the 3D composition impacts the dielectric environment of electron-hole pairs leading to electron-phonon interactions such as

charge carrier screening and phonon-assisted scattering; less is known regarding the nature of electron-phonon coupling and soft modes in 2D perovskites.[2g, 3] Organic spacer cations present in the 2D variants do not directly contribute to electronic band-edge transitions, but do intimately dictate the structure, symmetry and distortions of the metal halide octahedra, and can thus strongly influence the electronic properties.[4] Deviation from a 180° bond angle between the metal atoms and equatorial halides reduces overlap between the metal *s* and halide *p* orbitals, which blue-shifts the bandgap.[1c, 5] Both in-plane Pb-I-Pb angular distortions and out-of-plane octahedra tilt angles may play a role.[6] In most 2D perovskites, including those discussed in this work, the metal halide bond angles are distorted and considerably smaller than 180°.[1b, 1g]

Whereas the inorganic metal halide sublattice in 2D perovskites is crystallographically well-defined as signified by single crystal XRD, optical excitation can perturb the structure as electric fields change due to presence of electron-hole pairs that can lead to polaron formation and thermal energy arises from carrier cooling and relaxation.[4b, 4c, 7] Changes in locally available energy may cause perturbations of organic spacer cations as well as changes within the inorganic octahedra. Such influences suggest a complex landscape composed of interacting organic and inorganic components that is even influenced by the lone pair on the metal cation.[8] Furthermore, the soft, deformable nature of the inorganic sublattice, while bolstering defect tolerance, reduces comprehensive understanding of the static and dynamic properties of the material.[1a, 8b, 9]

To gain direct insight into the dynamic structural changes that occur upon photo-excitation and their potential impact on the carrier dynamics of the material in its excited state, we implement TrXRD as a function of pump fluence to study thin films of two canonical 2D perovskite compositions, $(BA)_2PbI_4$ and $(PEA)_2PbI_4$, which have been the focus of wide-ranging fundamental and applied studies. Using TrXRD, we collect picosecond-to-microsecond time-resolved PXRD patterns before and after above-bandgap photo-excitation.[10] We observe anisotropic lattice expansion as well as X-ray diffraction linewidth narrowing post-photo-excitation. These processes take place over the first 1 ns following photo-excitation without notable fluence dependence for the range of pump intensities studied, and each material returns to its static structure with two recovery time constants of approximately 3 nanoseconds and 400 nanoseconds. Unexpectedly, the (110) Bragg reflection in $(BA)_2PbI_4$, which is systematically absent in the crystal structure as reported previously by single crystal XRD, appears in TrXRD and undergoes pump-induced

expansion. Whereas such data suggests a transient non-equilibrium crystal lattice, upon further investigation of the static structure, we determine that the space group of this material is actually lower symmetry than previously reported and TrXRD data does not show a phase transition for the conditions examined.[1b]

We also perform variable temperature PXRD (VT-PXRD) which conveys that heating to the temperatures induced by TrXRD (increases of only a few Kelvin depending on fluence) causes a reduction of atomic order accompanied by very slight thermal expansion, contrasting with transient data that notably shows increased lattice order post-photo-excitation along with expansions that could not be caused by laser-induced temperature increases alone.[11] Time-resolved photoluminescence performed for fluences comparable to those measured in TrXRD, shows that the PL linewidths of both compositions narrow and redshift over approximately one nanosecond. Taken together, these data suggest that the distorted lead iodide octahedra within the inorganic layers of 2D perovskites undergo relaxation upon photo-excitation such that the Pb-I-Pb bond angles increase with increased ordering of octahedra, which give rise to observed redshifting and narrowing of the PL over time. Theoretical calculations of a quasi-cubic 2D perovskite structure corroborate our results, and suggest that optical pumping increases the out-of-plane Pb-I-Pb bond angles in $(BA)_2PbI_4$ (a decrease in the δ tilt angle) by approximately 5°. These results suggest that 2D perovskite lattices are sensitive to photo-excitation at low fluences, and that the formation of excitons is accompanied by changes in local structure and bonding that impact the emission efficiency and energy.

Results/Discussion

The orthorhombic $(BA)_2PbI_4$ crystal structure exhibits corner-sharing lead iodide octahedra that self-assemble in alternating layers with interdigitated butylammonium cations (Figure 1a, black).[1b] The ammonium moieties of the organic cations hydrogen-bond to iodine atoms in the inorganic sublattice such that the resulting Pb-I-Pb angles are approximately 155°, corresponding to in-plane β tilt angles of 12.5° and out of plane δ tilt angles of 5°, commensurate with a bandgap of 516 nm (2.4 eV) (Figure S2).[1k] $(PEA)_2PbI_4$ is similar structurally and electronically, except it crystallizes in a monoclinic space group (Figure S3).[1e] The transient TrXRD of $(BA)_2PbI_4$ (Figure 1a, Figure S4) contains features corresponding to the (002), (004), (111), (006), (008), and (0 0 10)

planes; we observe the same reflections in $(PEA)_2PbI_4$ except for the (111) and (0 0 10). In each material, the (002) planes bisect the lead and equatorial iodine atoms in the inorganic sublattices; the other (00*l*) (where $l = 2n$) peaks exhibit higher spatial frequencies than the (002) plane and bisect the organic cation layers (Figure 1b). The (111) plane of $(BA)_2PbI_4$ crosses the unit cell diagonally and therefore bisects both the inorganic and organic layers (Figure 1c). The crystal structures of both materials persist in these crystal phases well above room temperature (Figure S5).

Figures 2a and 2b show transient X-ray diffraction of the (002) plane of $(BA)_2PbI_4$ at 22 $\mu J/cm^2$ and 75 $\mu J/cm^2$, respectively, for the indicated pump-probe time delays. To best observe the processes occurring in the photo-excited material, we difference the post-photoexcitation PXRD patterns from the static PXRD patterns, resulting in a transient pattern containing positive and negative differential signals (details in SI). At both pump fluences, the positive and negative differential signal levels increase over the course of the first nanosecond following excitation, indicating that the (002) peak in the photo-excited structure shifts to lower Q over time. This signifies that the *c* axis expands, which we quantify by adding the differenced patterns to the original static pattern and examining the resultant reconstructed photo-excited pattern (details in SI). The interlayer direction undergoes maximum expansion of 0.17% at 22 $\mu J/cm^2$ and sub-linearly increases to 0.37% at 75 $\mu J/cm^2$ by 1 nanosecond (Figure 2c-d). In $(PEA)_2PbI_4$, the interlayer expands by 0.22% at 10 $\mu J/cm^2$, while expansion increases slightly at higher fluence to a maximum of 0.28% (Figure S7-S8) for the fluence range studied. These results suggest that expansion along the *c* axis here is not strongly cation-dependent, and is likely dictated by movement within the inorganic layers.

A second component of the observed differential transient diffraction is the relative amplitudes of the positive and negative differential signals s indicating changes in diffraction intensity post-photo-excitation. In $(BA)_2PbI_4$ at 22 $\mu J/cm^2$ (Figure 2a), the 120 ps and 200 ps time points each exhibit positive signals of lower intensity than the negative signals, indicating a net loss of diffraction intensity in the photo-excited structure at these times. By 800 ps, this post-excitation reduction in intensity is no longer evident, and the integrated areas of the positive and negative signals become approximately equal and, by 1 ns the positive signal is clearly larger than the negative signal. This relative increase in positive amplitude of the (002) peak indicates that the

photo-excited material diffracts more strongly at this time than the static material and that the FWHM post-photo-excitation has narrowed.

At 75 μJ/cm^2, the positive signal of the differential TrXRD in $(BA)_2PbI_4$ is higher in amplitude than the negative signal at earlier times, starting from 120 ps, suggesting that changes in the Pb-I-Pb bond angles and extent of octahedral distortions are fluence-dependent (Figure 2b). This fluence dependence may arise from changes in how much of the sample undergoes photoexcitation; at higher fluences, enough sample may be photoexcited such that there is an increase in long range order that is not observed at lower fluences until later delay times. Transient changes in bond angles are discussed in more detail below. The processes observed at both fluences are reversible, as by 50 ns these changes have mostly recovered, and the derivative line shapes are approximately symmetric (Figure 2a-b). The data in Figure 2a-b is summarized in the inset of Figure 2b (the dashed line indicates $\int \Delta S = 0$). We investigated additional fluences at 300 ps and 1 ns, and observe that at 300 ps the diffraction intensity reduction persists for lower fluences, but by 1 ns intensity increases are observed for all examined fluences (Figure S6). Regardless of fluence, maximum signal in $(BA)_2PbI_4$ is reached at 1 nanosecond. In $(PEA)_2PbI_4$, maximal transient signal is reached at approximately 800 ps, a shorter delay time than for $(BA)_2PbI_4$, suggesting that lattice reorganization is faster within the more rigid phenethylammonium cations. A slight increase in post-excitation diffraction intensity along the (002) plane is observed at low fluences, and this effect increases with fluence (Figure S8), which suggests that the structural ordering or disordering observed in 2D metal halide perovskites depend on the organic spacer cation, as post-excitation loss of peak intensity is not observed in $(PEA)_2PbI_4$.

For both $(BA)_2PbI_4$ and $(PEA)_2PbI_4$, the high angle (00*l*) planes behave similarly to the (002), as is expected within a family of planes. Figure S9 shows time-dependent TrXRD data of higher-index in-plane directions of $(BA)_2PbI_4$ at 75 μJ/cm^2; the corresponding high-angle data for $(PEA)_2PbI_4$ is in Figure S10. We examine the (00*l*) planes where l = 4, 6, 8, or 10, all of which bisect the organic cations and therefore probe local order within the organic lattice. Like the (002) planes, there is slight expansion along the higher angle planes at 40 ps, which grows over time and reaches a maximum at 1 ns. At longer time delays, we observe slightly larger positive signalss, suggesting a transient increase in long-range lattice coherence on the same timescale as is observed within the (002) planes.

As 2D perovskite thin films have a strong degree of preferential orientation for the (00*l*) reflections, it proved difficult to experimentally observe out-of-plane reflections which could give more conclusive insight regarding changes in atomic ordering that we observe from the in-plane reflections. Due to insufficient signal-to-noise, it is difficult to determine the relative ratios of positive to negative transient signal and we therefore cannot make conclusive statements as to any ordering or disordering processes occurring in this direction. However, we can see that the (111) plane in $(BA)_2PbI_4$ undergoes some modest amount of thermal expansion (Figure 3a), and, using the same method as described above, we determined this expansion to be 0.03%, a factor of 10 smaller than the interlayer expansion.

These results strongly suggest that the effects observed post-photo-excitation are due in large part to formation of excitons, but the full impact of above-bandgap photo-excitation is unclear. It is possible that the excess thermal energy resulting from the formation of hot carriers aids in relaxation of the distorted lead iodide octahedra and induces subsequent expansion and increases in long range coherence, as seen in the increased diffraction post-photo-excitation of the (002) planes. Previous reports have shown that the anti-bonding character of the valence band contributes to the distortion of in-plane Pb-I-Pb bond angles and δ octahedral tilts in the static structure, which further bolsters our hypothesis that photo-excitation of electrons across the bandgap can relieve lattice distortions.[5a] This post-photo-excitation relaxation of the octahedral bond angles and subsequent increase in bond strength between lead and iodine atoms may be responsible for the increased intensity and reduced FWHM of (00*l*) diffraction peaks within the inorganic lattice.

To differentiate the impact of thermal energy produced from carrier relaxation vs. exciton formation on the structural changes observed in TrXRD, we measured VT-PXRD of $(BA)_2PbI_4$. We chose measurement parameters by calculating temperatures that may be accessed by photo-excitation with the 400 nm pump used in the transient XRD experiment (Figure S11). These calculations suggest that changes in temperature induced by the pump are only a few degrees Kelvin even at high pump fluences. Extrema assumptions estimate either that the entirety of the pump photon energy goes into thermal energy (high effective ΔT) or that only the energy above-gap is converted to thermal energy (low effective ΔT) (Figure S11).

Our VT-PXRD measurements (Figure S12) show that increasing temperature by a few Kelvin leads to shifts of the (002), (004), and (111) reflections to lower Q, and that peak intensity deceases. These static measurements convey heating causes the material to both expand and lose atomic order as expected from Debye-Waller factors, in contrast to the expansion and distortion relaxation processes observed with TrXRD. Assuming that the low ΔT model is more accurate, the temperature change induced by laser pumping is very small regardless of fluence, at about 2 K for $(BA)_2PbI_4$ at 75 μJ/cm^2. The expansion induced along the (002) plane by a 2 K increase in temperature (300 K → 302 K) in VT-PXRD is only 0.031%, which is considerably smaller than the expansions of 0.17%-0.37% we observe post-photo-excitation in TrXRD. Taken together, this suggests that photo-excited electronic states, not excess thermal energy, are principally responsible for lattice dynamics observed for the (00*l*) peaks.

Interestingly. Figure 3a shows transient expansion of an unexpected peak that is reported to be systematically absent in the static structure of $(BA)_2PbI_4$.[1b] The (111) plane (1.05 Å^{-1}), which diagonally bisects the inorganic and organic sublattices, undergoes thermal expansion for the first ~200 ps of the measurement, followed by the emergence of a weaker second peak at slightly lower Q. This second peak is not obvious in static X-ray diffraction, and, given the understood structure, is likely the systematically absent (110) reflection due to match with the simulated powder pattern.[1b] Proximity of these two diffraction features makes a clear understanding of their relative dynamics difficult, but would suggest that 1) creation of electron-hole pairs induces shifting within the 2D crystal structure such that symmetry of the orthorhombic phase is broken when out of equilibrium, allowing the (110) plane to appear transiently or 2) the static crystal structure of $(BA)_2PbI_4$ is of lower symmetry than previously determined using single crystal diffraction.

To determine the origin of this unrecognized peak, we collected single crystal X-ray diffraction data on $(BA)_2PbI_4$ to first confirm the structure determination made in earlier reports. To aid in this, we obtained higher intensity data than in previous reports using, a combination of a bright X-ray source and highly sensitive detector in combination with collecting data on a larger single crystal than in the previous reports of the material structure. Unexpectedly, we observed numerous reflections including the (110) reflection in the static, room temperature structure that collectively violate the systematic absence conditions that are the result of three glide planes present in the previously reported *Pbca* space group. The synthesized precession images from the single

crystal data down the [100], the [010], and the [001] directions are shown in Figure S13. The specific set of reflection conditions that would be systematically absent due to the glide planes in *Pbca* are the (0kl) when k = 2n, the (h0l) when l = 2n, and the (hk0) when h = 2n (details in SI). To confirm our results, multiple crystals from two different synthetic batches were studied, and these reflections were observable with a sufficiently large crystal (L,W, H > 50 μm) in the beam path. Examination of the report by Billing and Lemmerer indicates that the intensity data they obtained was insufficient to observe these weakly diffracting reflections that violate the glide planes.[1b] Based on an extinction analysis of the single crystal data, the lower symmetry orthorhombic space group $P2_12_12_1$ is selected as the new space group for the static structure of $(BA)_2PbI_4$. Since the (110) reflection is not systematically absent in the static structure of $(BA)_2PbI_4$, this means that our observation of this reflection in the transient XRD experiment is not indicative of a change in symmetry due to photo-excitation. A new electronic band structure calculation of the material in the $P2_12_12_1$ space group reveals that the symmetry change negligibly changes the energy gap (2.79 eV vs 2.80 eV) (Figure S19), although the change in inversion symmetry does raise prospects for utility in nonlinear optical or ferroelectric applications.

In contrast to the photo-excited structural behavior observed in colloidal nanoparticle systems, it is noteworthy that a measurable increase in transient signal appears over time for the perovskites studied here, and the largest shift in Q for the (002) diffraction peak in both materials is not reached until approximately 700 ps–1 ns.[10a-c] This suggests that the inorganic layers undergo slow relaxation processes that do not reach a quasi-equilibrium for close to a nanosecond. To quantify the expansion, we integrated the area under the absolute value of the differenced curves at each time delay to produce rise and recovery dynamics. During the first nanosecond, two processes occur in both $(BA)_2PbI_4$ and $(PEA)_2PbI_4$ – one from 40 ps-500 ps, and a subsequent process from 500 ps-1 ns (Figure 4a, Figure S14a). The same phenomenon occurs in the higher order planes of $(BA)_2PbI_4$ (Figure 4c) and $(PEA)_2PbI_4$ (Figure S14a) as in the (002) reflections, suggesting that the rise in each of these is governed by these two same processes. This behavior is again suggestive of a transient change in the crystal structure. We believe that the first process involves expansion of the *c* axis in the first ~500 ps, followed by a decrease in octahedral distortions among the lead iodide octahedra between ~500 ps and 1 ns.

Recovery of the (002) plane in $(BA)_2PbI_4$ following 22 μJ/cm^2 excitation was fit to a biexponential equation, which yielded time constants τ_1 of 2.6 ± 0.6 ns and τ_2 of 333 ± 71 ns (Figure 4b). These lifetimes follow relaxation of the distorted lead iodide octahedra and subsequent cooling of the photo-excited lattice. They are not significantly fluence-dependent in the examined regime (Figure 4b), bolstering our hypothesis that excited electron-hole pairs distort the static structure with considerably more force than would be observed with thermal energy alone. The same process was followed to obtain dynamics at 75 μJ/cm^2 of the (004), (006), (008), and (0010) planes after 1 ns (Figure 4d). The (004) plane recovers with τ_1 of 2.3 ± 0.5 ns and τ_2 of 432 ± 57 ns, similar to the lifetimes observed in the (002) plane. The remaining high-angle planes recover on similar timescales, suggesting that the dynamics of these planes are dominated by processes occurring in the inorganic sublattice, or the (002) plane. In $(PEA)_2PbI_4$, the recovery timescales of the (002) plane (τ_1 = 2.7 ± 0.5 ns and τ_2 = 350 ± 39 ns) are, perhaps surprisingly, very similar to those observed in $(BA)_2PbI_4$, suggesting that recovery is mostly dependent on the lead iodide sublattice and is only weakly affected by the organic cations (Figure S14b). Within the high angle multiples, the timescales are similar to each other as well as the timescales observed in $(BA)_2PbI_4$. These long timescales go well beyond any electronic effects that could be observed due to photoexcitation, and are therefore attributable to non-equilibrium changes in the crystallinity of the materials. We hypothesize that, after the initial photoexcitation and reorganization that takes approximately 1 ns, the non-equilibrium structure recovers on long timescales, possibly due to relatively weak energetic potentials. The materials eventually return to their static structures.

Even minor changes in the crystal structures of 2D perovskites, such as the ordering and disordering we report here, can cause the emission and absorption to shift if there are changes in the Pb-I-Pb bonding as we have demonstrated. In order to investigate potential electronic changes related to our crystallographic findings, we measured time- and fluence-dependent photoluminescence of $(BA)_2PbI_4$ (Figure 5, Figure S15-16) and $(PEA)_2PbI_4$ (Figure S17) using a streak camera. We note that, while defects may impact some aspects of time-resolved photoluminescence analysis, we do not expect these to have a significant impact on fluence-dependent observations. At pump fluences of 24-234 μJ/cm^2, similar to those investigated using TrXRD, we note narrowing of the PL emission in both materials that occurs over the first 500 ps following excitation, and the FWHM of each diffraction plane within this time window decreases.

These changes are particularly evident when comparing the static and early (<500 ps) PL to late PL (>1 ns) (Figure 5a). The decrease in FWHM (Figure 5a-b) is consistent with the observed increase of diffraction in the first 1 ns observed in TrXRD within the (002) plane (Figure 2a-b, Figure S8), suggesting that this phenomenon is largely dictated by charge carrier generation and not solely by thermal energy (it is worth noting that, at the fluences shown in Figure 2, we are likely not accessing a Mott transition, and therefore we believe that electron-hole pairs, not an exciton plasma, are responsible for our observations).[12] The FWHM of the transient PL changes with fluence at early times, but has very little fluence dependence at 1 and 2 nanoseconds, similar to the trends observed in TrXRD. Additionally, the observed 500 ps timescale may relate to the two processes observed in the TrXRD data occurring at 500 ps and 1 ns (Figure 4a, Figure S14a). We observe the FWHM of the PL narrowing over 2 ns in both perovskites, a similar timescale to the τ_1 of 2.6 ns and 2.7 ns calculated for the relaxation process from TrXRD, suggesting that this is the lifetime of evolution toward relaxed Pb-I-Pb bond angles. The PL decay lifetimes of both perovskites are shorter than those observed in TrXRD; however, both materials emit past 1 ns (Figure S18), suggesting that there are still excitons present in the films studied with TrXRD well after they have begun cooling.

To further bolster our hypothesis that photo-excitation induces relaxation of the inorganic octahedra and bandgap redshifting, we compared experimental results with calculation. Specifically, we considered the electronic structure of the material at the best affordable level of DFT using the HSE06 hybrid functional including spin-orbit coupling (Figure S19), in both the static state and a theoretical D4h model structure, Cs_2PbI_4. In this maximally symmetrized structure, all in-plane Pb-I-Pb bond angles have been artificially fixed to 180° and δ tilt angles reduced to 0°, which provides us with some approximation of how a fully relaxed structure relative to the static structure may behave. It is worth noting that the static structures used for calculations are not a perfect comparison to the non-equilibrium conditions that we probe experimentally. Earlier theoretical work suggests that small changes in the in-plane bond angles, such as the 0.03% expansion observed in TrXRD, leads only to slight modifications of the bandgap, consistent with our observations using TrPL.[6] The slight redshifting of emission wavelengths is expected upon relaxation of the lead iodide octahedra, and not by simultaneous reductions of the in-plane and out-of-plane tilt angles that would yield much larger redshifts. Instead, this work suggests that, given

the expansions we observe from TrXRD, there is significant change of the out-of-plane angles, and a minor change of the in-plane angles. These calculations indicate that expansions in the out-of-plane direction solely related to change in tilt angles would lead to a larger change of the optical bandgap than is observed in our data; however, this discrepancy likely arises due to differences between the calculated structure and the probed non-equilibrium atomic configuration. Given the observed bandgap redshift of approximately 5 nm (+/- 1 nm) by 1-2 ns observed for $(BA)_2PbI_4$, we expect from these calculations that the out-of-plane Pb-I-Pb bond angles increase (the δ tilt angles decrease) approximately by 5° (Figure S20) to approach 160°.

Conclusion

Taken together, our data suggest that 2D perovskite thin films photo-excited at room temperature exhibit changes in atomic order that directly influence electronic transition energies. Following photo-excitation, the lattices of $(BA)_2PbI_4$ expands in the *c* direction by up to 0.37%, and in the *ab* plane by 0.03%. $(PEA)_2PbI_4$ undergoes similar expansion along the *c* axis. Both perovskites undergo an increase in diffraction in the (002) plane in the first nanosecond after excitation, likely a result of the statically distorted Pb-I-Pb bonds angles, initially at 155°, to evolve toward 160° in the out-of-plane direction (a reduction of the out-of-plane tilt angle as calculated for $(BA)_2PbI_4$ based on DFT). This effect appears to be weakly dependent on the organic spacer cation, as some decrease in diffraction is observed at early times and low fluences in $(BA)_2PbI_4$ but not in $(PEA)_2PbI_4$. Rise and recovery dynamics are calculated and found to be very similar between the two materials, with the exception of the expansion in $(BA)_2PbI_4$ being approximately 200 ps slower than in $(PEA)_2PbI_4$. We find that the effects observed here are due in large part to photo-excitation of charge carriers, as we do not observe the same changes in variable temperature static PXRD. In transient measurements, we observe the development of a differential signal corresponding to the (110) plane in $(BA)_2PbI_4$ that was previously understood to be systematically absent. We further investigated and discern that the actual static crystal structure of this material is of lower symmetry than previously reported. We resolve the crystal structure and determine that it belongs to the $P2_12_12_1$ space group, and thereby also rule out a photoinduced, symmetry-changing, non-equilibrium phase transition. Time-resolved photoluminescence measurements and DFT calculations provide further insight regarding the diffraction changes observed in TrXRD, and support our determination that these dynamic lattice effects are largely photoinduced. With these,

we ascertain that, over 2 ns post-photo-excitation, the FWHMs of emission linewidths decrease and emission energy redshifts as lattice ordering transiently increases.

Acknowledgements

This research used resources of the Advanced Photon Source, a U.S. Department of Energy (DOE) Office of Science User Facility, operated for the DOE Office of Science by Argonne National Laboratory under Contract No. DE-AC02-06CH11357. This work was performed, in part, at the Center for Nanoscale Materials, a Department of Energy Office of Science User Facility, and supported by the U.S. DOE, Office of Basic Energy Sciences, under Contract No. DE-AC02-06CH11357. At Northwestern University, this work is supported by the Department of Energy, Office of Science, Basic Energy Sciences, under Grant No. SC0012541 (M.G.K., synthesis, structure, and characterization of physical properties) and by the National Science Foundation Macromolecular, Supramolecular, and Nanochemistry award #1808590 for elevated fluence optical investigation. This work made use of the IMSERC facility at Northwestern University, which has received support from the Soft and Hybrid Nanotechnology Experimental (SHyNE) Resource (NSF ECCS-2025633), and Northwestern University. Purchase of the Ag-microsource diffractometer used to obtain results included in this publication was supported by the Major Research Instrumentation Program from the National Science Foundation under the award CHE-1920248. This material is based upon work supported by the National Science Foundation Graduate Research Fellowship Program under Grant No. DGE-1842165 (S.P. and A.B.). A.M.L. acknowledges support from by the Department of Energy, Office of Science, Basic Energy Sciences, Materials Sciences and Engineering Division, under Contract DE-AC02-76SF00515. This work was performed with financial support from the European Union's Horizon 2020 program through an Innovation Action under grant agreement no. 861985 (PEROCUBE). J.E. acknowledges financial support from the Institute Universitaire de France. This work was granted access to the HPC resources of [TGCC/CINES/IDRIS] under the allocations 2020-A0100911434 and 2020-A0090907682 made by GENCI.

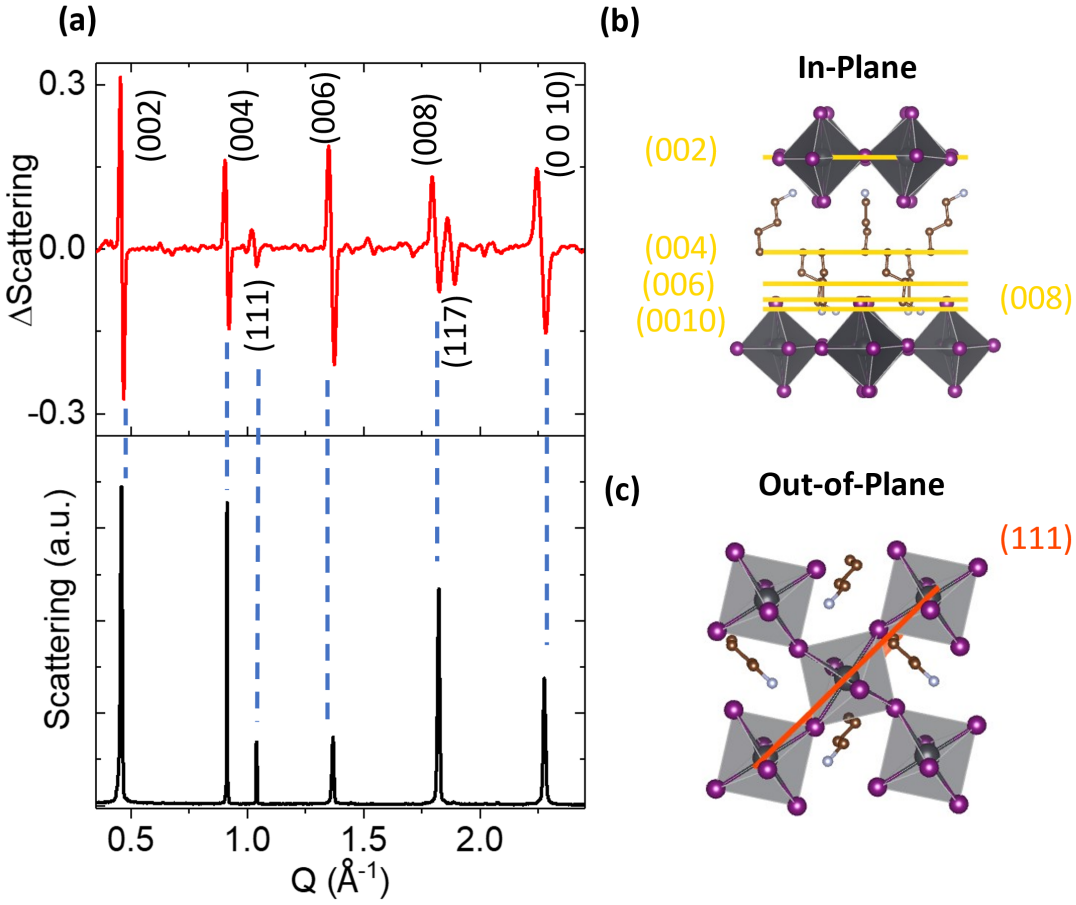

Figure 1: (a) Static XRD pattern (black) and transient (pump-on minus pump-off, here at 1 ns and 22 μJ/cm^2, red) X-ray diffraction of $(BA)_2PbI_4$. Note that in the static pattern, the (117) plane is not clearly visible due to low intensity. In-plane (b) and out-of-plane (c) peaks of interest for this study. The structures in (b) and (c) were taken from previously published crystallographic data.

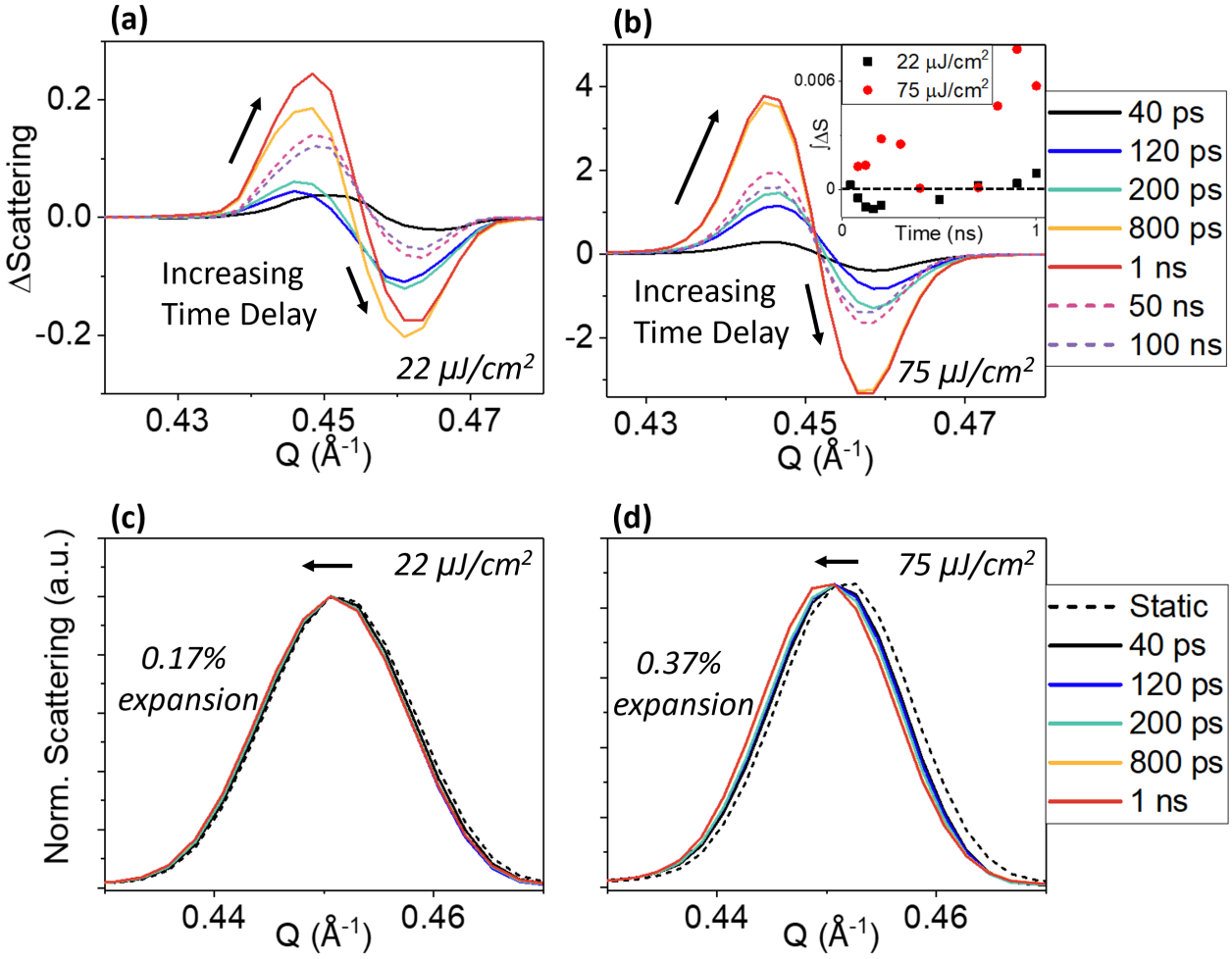

Figure 2: Differenced scans of the 002 plane of $(BA)_2PbI_4$ at (a) 22.1 μJ/cm^2 and (b) 75 μJ/cm^2 showing thermal expansion and ordering over a nanosecond. Inset is the integrated ΔS curves at the same fluences and time delays, showing slight disordering at early times and low fluence, and ordering at all time delays at the higher fluence (dashed line shows $\int\Delta S = 0$). (c) and (d) show the static and post-photo-excitation PXRD peaks obtained by adding the differenced data back to static data, and show fluence-dependent expansion along the stacking direction.

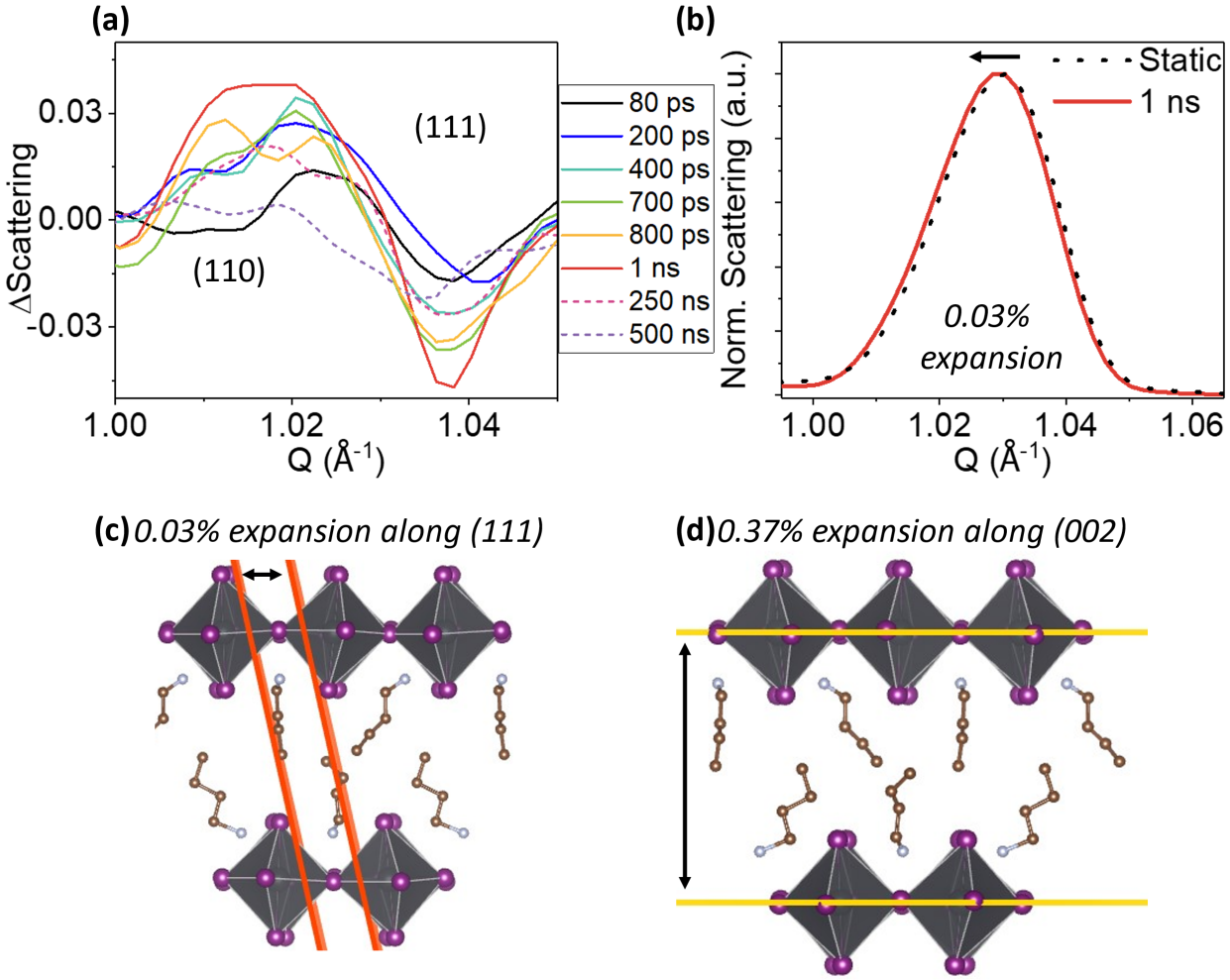

Figure 1: (a) shows the (111) plane of $(BA)_2PbI_4$ at approximately Q = 1.03 overlapping with the (110) plane at approximately Q = 1.02 (data taken at 75 uJ/cm^2). While it is difficult to determine the extent of positive to negative differential signals s from this data due to low signal/noise and planes overlapping, both appear to undergo thermal expansion. Expansion in the (111) reflection has been quantified in (b), which shows the (111) peak shifting to slightly lower Q at 1 ns post-excitation. This direction expands by 0.03% (c) as compared to a factor of 10 increase of 0.37% in the (002) direction (d).

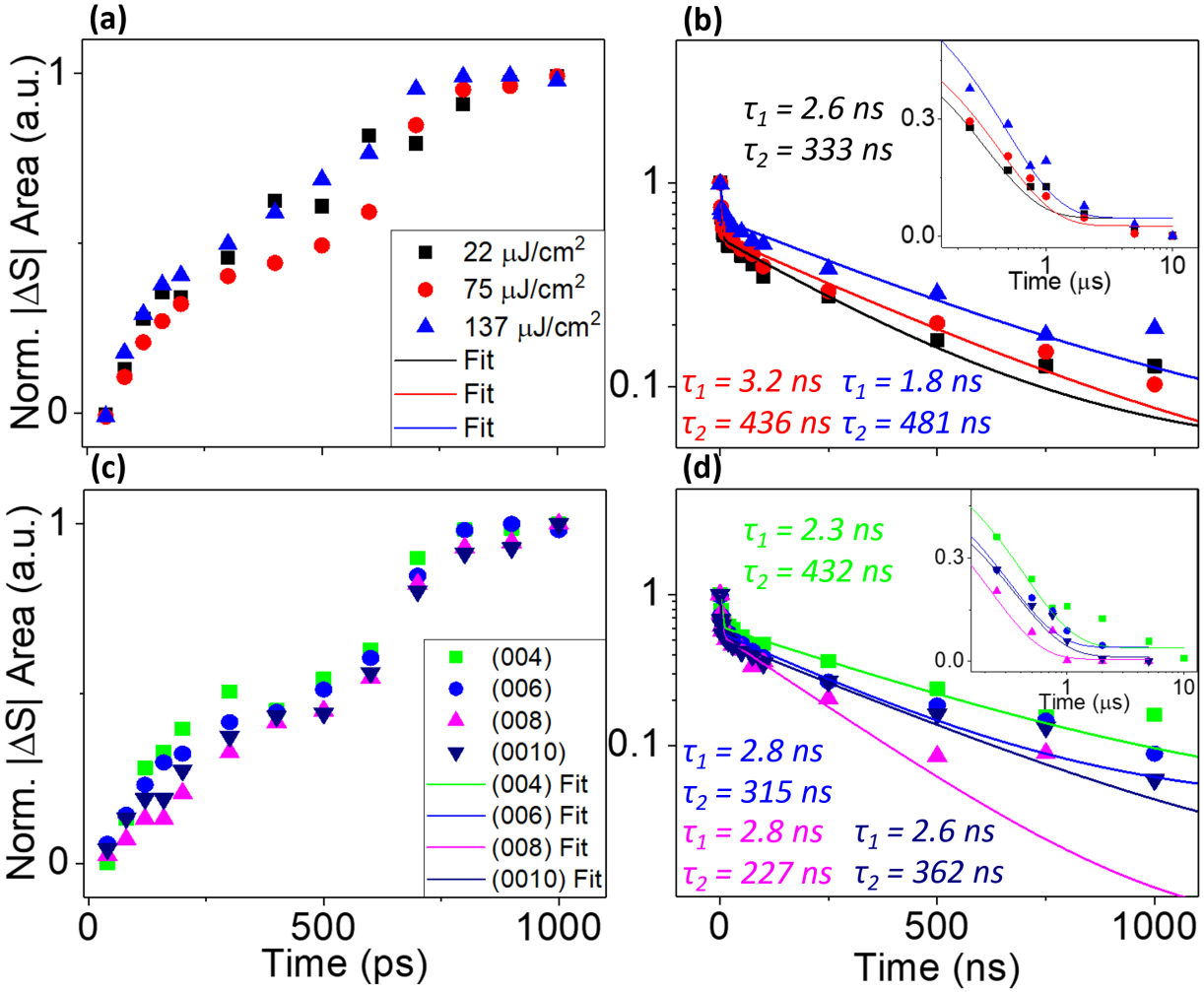

Figure 4: Dynamics of structural changes along the (002) reflection of $(BA)_2PbI_4$ at 22 μJ/cm^2, 75 μJ/cm^2, and 137 μJ/cm^2 showing both the rise (a) and the recovery (b); these are determined by taking the area under the absolute value of the differenced curves at each time delay. The rise and recovery of the (004), (006), (008), and (0010) planes of $(BA)_2PbI_2$ at 75 μJ/cm^2 are shown in (c) and (d). Solid lines indicate biexponential fits. The time constants do not change significantly between fluence or reflection of interest, suggesting that the dynamics are fluence-independent and that the behavior of the higher angle planes is dictated by that of the (002).

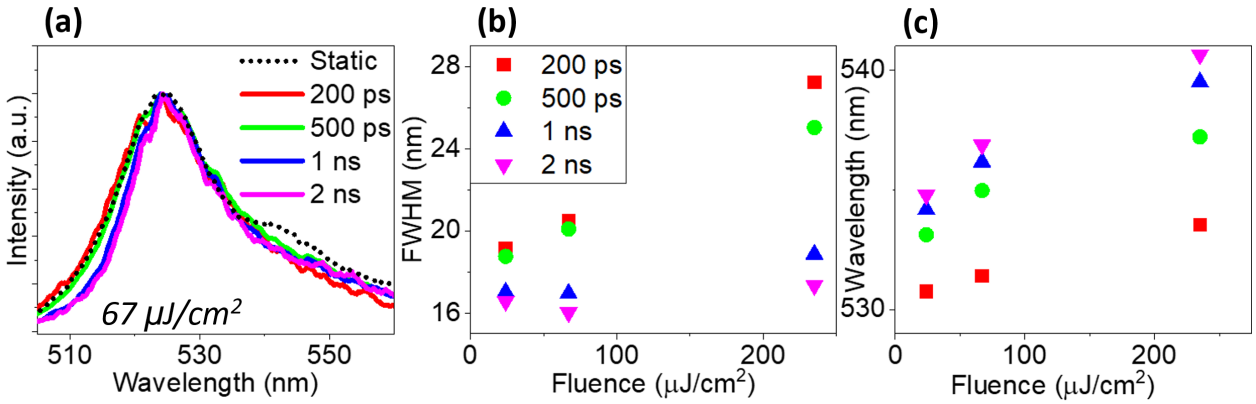

Figure 5: Time-resolved photoluminescence spectra of $(BA)_2PbI_4$ at 67 μJ/ cm^2 normalized to 1 (a). The static data in (a) was taken using CW laser excitation. FWHM (b) and centroid (c) of the emission with respect to wavelength and time showing that the emission narrows and redshifts over time and as fluence increases.

Conflicts of Interest

The authors declare no conflicts of interest.

References

[1] a)C. M. Mauck, A. France-Lanord, A. C. Hernandez Oendra, N. S. Dahod, J. C. Grossman, W. A. Tisdale, *The Journal of Physical Chemistry C* **2019**, 123, 27904; b)D. G. Billing, A. Lemmerer, **2007**, 63, 735; c)T. Ishihara, J. Takahashi, T. Goto, *Physical Review B* **1990**, 42, 11099; d)W. Paritmongkol, E. R. Powers, N. S. Dahod, W. A. Tisdale, *The Journal of Physical Chemistry Letters* **2020**, 8565; e)K.-z. Du, Q. Tu, X. Zhang, Q. Han, J. Liu, S. Zauscher, D. B. Mitzi, *Inorganic Chemistry* **2017**, 56, 9291; f)D. B. Mitzi, *Journal of the Chemical Society, Dalton Transactions* **2001**, 1; g)D. B. Mitzi, *Chemistry of Materials* **1996**, 8, 791; h)Z.-K. Tan, R. S. Moghaddam, M. L. Lai, P. Docampo, R. Higler, F. Deschler, M. Price, A. Sadhanala, L. M. Pazos, D. Credgington, F. Hanusch, T. Bein, H. J. Snaith, R. H. Friend, *Nature Nanotechnology* **2014**, 9, 687; i)B. R. Sutherland, E. H. Sargent, *Nature Photonics* **2016**, 10, 295; j)W. Zhang, G. E. Eperon, H. J. Snaith, *Nature Energy* **2016**, 1, 16048; k)C. C. Stoumpos, D. H. Cao, D. J. Clark, J. Young, J. M. Rondinelli, J. I. Jang, J. T. Hupp, M. G. Kanatzidis, *Chemistry of Materials* **2016**, 28, 2852.

[2] a)P. Guo, C. C. Stoumpos, L. Mao, S. Sadasivam, J. B. Ketterson, P. Darancet, M. G. Kanatzidis, R. D. Schaller, *Nature Communications* **2018**, 9, 2019; b)M. D. Smith, B. A. Connor, H. I. Karunadasa, *Chemical Reviews* **2019**, 119, 3104; c)K. Tanaka, F. Sano, T. Takahashi, T. Kondo, R. Ito, K. Ema, *Solid State Communications* **2002**, 122, 249; d)O. Yaffe, A. Chernikov, Z. M. Norman, Y. Zhong, A. Velauthapillai, A. van der Zande, J. S. Owen, T. F. Heinz, *Physical Review B* **2015**, 92, 045414; e)N. Kitazawa, M. Aono, Y. Watanabe, *Materials Chemistry and Physics* **2012**, 134, 875; f)F. Thouin, S. Neutzner, D. Cortecchia, V. A. Dragomir, C. Soci, T. Salim, Y. M. Lam, R. Leonelli, A. Petrozza, A. R. S. Kandada, C. Silva, *Physical Review Materials* **2018**, 2, 034001; g)M. Menahem, Z. Dai, S. Aharon, R. Sharma, M. Asher, Y. Diskin-Posner, R. Korobko, A. M. Rappe, O. Yaffe, *ACS Nano* **2021**, 15, 10153.

[3] a)C. La-o-vorakiat, H. Xia, J. Kadro, T. Salim, D. Zhao, T. Ahmed, Y. M. Lam, J.-X. Zhu, R. A. Marcus, M.-E. Michel-Beyerle, E. E. M. Chia, *The Journal of Physical Chemistry Letters* **2016**, 7, 1; b)T. Lanigan-Atkins, X. He, M. J. Krogstad, D. M. Pajerowski, D. L. Abernathy, G. N. M. N. Xu, Z. Xu, D. Y. Chung, M. G. Kanatzidis, S. Rosenkranz, R. Osborn, O. Delaire, *Nature Materials* **2021**, 20, 977; c)R. F. Moral, J. C. Germino, L. G. Bonato, D. B. Almeida, E. M. Therézio, T. D. Z. Atvars, S. D. Stranks, R. A. Nome, A. F. Nogueira, *Advanced Optical Materials* **2020**, n/a, 2001431; d)Y. Lan, B. J. Dringoli, D. A. Valverde-Chávez, C. S. Ponseca, M. Sutton, Y. He, M. G. Kanatzidis, D. G. Cooke, *Science Advances* **2019**, 5, eaaw5558.

[4] a)C. Li, J. Yang, F. Su, J. Tan, Y. Luo, S. Ye, *Nature Communications* **2020**, 11, 5481; b)N. S. Dahod, W. Paritmongkol, A. Stollmann, C. Settens, S.-L. Zheng, W. A. Tisdale, *The Journal of Physical Chemistry Letters* **2019**, 10, 2924; c)X. Li, J. M. Hoffman, M. G. Kanatzidis, *Chemical Reviews* **2021**, 121, 2230; d)M. A. J. Rasel, A. Giri, D. H. Olson, C. Ni, P. E. Hopkins, J. P. Feser, *ACS Applied Materials & Interfaces* **2020**, 12, 53705.

[5] a)J. L. Knutson, J. D. Martin, D. B. Mitzi, *Inorganic Chemistry* **2005**, 44, 4699; b)J.-H. Lee, N. C. Bristowe, J. H. Lee, S.-H. Lee, P. D. Bristowe, A. K. Cheetham, H. M. Jang, *Chemistry of Materials* **2016**, 28, 4259.

[6] L. Pedesseau, D. Sapori, B. Traore, R. Robles, H.-H. Fang, M. A. Loi, H. Tsai, W. Nie, J.-C. Blancon, A. Neukirch, S. Tretiak, A. D. Mohite, C. Katan, J. Even, M. Kepenekian, *ACS Nano* **2016**, 10, 9776.

[7] D. Niesner, H. Zhu, K. Miyata, P. P. Joshi, T. J. S. Evans, B. J. Kudisch, M. T. Trinh, M. Marks, X. Y. Zhu, *Journal of the American Chemical Society* **2016**, 138, 15717.

[8] a)L. Gao, L. Yadgarov, R. Sharma, R. Korobko, K. M. McCall, D. H. Fabini, C. C. Stoumpos, M. G. Kanatzidis, A. M. Rappe, O. Yaffe, *Materials Advances* **2021**; b)B. Guzelturk, T. Winkler, T. W. J. Van de Goor, M. D. Smith, S. A. Bourelle, S. Feldmann, M. Trigo, S. W. Teitelbaum, H.-G. Steinrück, G. A. de la Pena, R. Alonso-Mori, D. Zhu, T. Sato, H. I. Karunadasa, M. F. Toney, F. Deschler, A. M. Lindenberg, *Nature Materials* **2021**, 20, 618.

[9] a)D. A. Egger, A. M. Rappe, L. Kronik, *Accounts of Chemical Research* **2016**, 49, 573; b)X. Wu, L. Z. Tan, X. Shen, T. Hu, K. Miyata, M. T. Trinh, R. Li, R. Coffee, S. Liu, D. A. Egger, I. Makasyuk, Q. Zheng, A. Fry, J. S. Robinson, M. D. Smith, B. Guzelturk, H. I. Karunadasa, X. Wang, X. Zhu, L. Kronik, A. M. Rappe, A. M. Lindenberg, *Science Advances* **2017**, 3, e1602388; c)J. M. Frost, A. Walsh, *Accounts of Chemical Research* **2016**, 49, 528; d)C. Quarti, E. Mosconi, F. De Angelis, *Physical Chemistry Chemical Physics* **2015**, 17, 9394; e)L. Piveteau, M. Aebli, N. Yazdani, M. Millen, L. Korosec, F. Krieg, B. M. Benin, V. Morad, C. Piveteau, T. Shiroka, A. Comas-Vives, C. Copéret, A. M. Lindenberg, V. Wood, R. Verel, M. V. Kovalenko, *ACS Central Science* **2020**, 6, 1138; f)P. Guo, J. Gong, S. Sadasivam, Y. Xia, T.-B. Song, B. T. Diroll, C. C. Stoumpos, J. B. Ketterson, M. G. Kanatzidis, M. K. Y. Chan, P. Darancet, T. Xu, R. D. Schaller, *Nature Communications* **2018**, 9, 2792; g)K. Miyata, T. L. Atallah, X.-Y. Zhu, **2017**, 3, e1701469; h)Y. Liu, B. G. Sumpter, J. K. Keum, B. Hu, M. Ahmadi, O. S. Ovchinnikova, *ACS Applied Energy Materials* **2021**, 4, 2068.

[10] a)A. Brumberg, M. S. Kirschner, B. T. Diroll, K. R. Williams, N. C. Flanders, S. M. Harvey, A. A. Leonard, N. E. Watkins, C. Liu, E. D. Kinigstein, J. Yu, A. M. Evans, Y. Liu, S. A. Cuthriell, S. Panuganti, W. R. Dichtel, M. G. Kanatzidis, M. R. Wasielewski, X. Zhang, L. X. Chen, R. D. Schaller, *Nano Letters* **2021**, 21, 1288; b)B. T. Diroll, A. Brumberg, A. A. Leonard, S. Panuganti, N. E. Watkins, S. A. Cuthriell, S. M. Harvey, E. D. Kinigstein, J. Yu, X. Zhang, M. G. Kanatzidis, M. R. Wasielewski, L. X. Chen, R. D. Schaller, *Nanoscale* **2021**, 13, 2658; c)M. S. Kirschner, B. T. Diroll, P. Guo, S. M. Harvey, W. Helweh, N. C. Flanders, A. Brumberg, N. E. Watkins, A. A. Leonard, A. M. Evans, M. R. Wasielewski, W. R. Dichtel, X. Zhang, L. X. Chen, R. D. Schaller, *Nature Communications* **2019**, 10, 504; d)M. S. Kirschner, D. C. Hannah, B. T. Diroll, X. Zhang, M. J. Wagner, D. Hayes, A. Y. Chang, C. E. Rowland, C. M. Lethiec, G. C. Schatz, L. X. Chen, R. D. Schaller, *Nano Letters* **2017**, 17, 5314; e)S. M. Harvey, D. W. Houck, M. S. Kirschner, N. C. Flanders, A. Brumberg, A. A. Leonard, N. E. Watkins, L. X. Chen, W. R. Dichtel, X. Zhang, B. A. Korgel, M. R. Wasielewski, R. D. Schaller, *ACS Nano* **2020**, 14, 13548; f)W. Li, S. Sidhik, B. Traore, R. Asadpour, J. Hou, H. Zhang, A. Fehr, J. Essman, Y. Wang, J. M. Hoffman, I. Spanopoulos, J. J. Crochet, E. Tsai, J. Strzalka, C. Katan, M. A. Alam, M. G. Kanatzidis, J. Even, J.-C. Blancon, A. D. Mohite, *Nature Nanotechnology* **2022**, 17, 45.

[11] a)A. Giri, A. Z. Chen, A. Mattoni, K. Aryana, D. Zhang, X. Hu, S.-H. Lee, J. J. Choi, P. E. Hopkins, *Nano Letters* **2020**, 20, 3331; b)B. Song, J. Hou, H. Wang, S. Sidhik, J. Miao, H. Gu, H. Zhang, S. Liu, Z. Fakhraai, J. Even, J.-C. Blancon, A. D. Mohite, D. Jariwala, *ACS Materials Letters* **2021**, 3, 148.

[12] a)G. Delport, G. Chehade, F. Lédée, H. Diab, C. Milesi-Brault, G. Trippé-Allard, J. Even, J.-S. Lauret, E. Deleporte, D. Garrot, *The Journal of Physical Chemistry Letters* **2019**, 10, 5153; b)K. Zheng, Y. Chen, Y. Sun, J. Chen, P. Chábera, R. Schaller, M. J. Al-Marri, S. E. Canton, Z. Liang, T. Pullerits, *Journal of Materials Chemistry A* **2018**, 6, 6244.

TOC

The non-equilibrium crystal structures of 2D lead iodide perovskites are studied using ultrafast pump-probe X-ray diffraction. It is observed that PXRD peaks post-photoexcitation increase in intensity and narrow over 1 ns, suggesting an increase in long range order within the lead iodide octahedra. These results are corroborated using ultrafast photoluminescence, which shows a redshifting and narrowing of PL peaks on the same timescale as TrXRD.

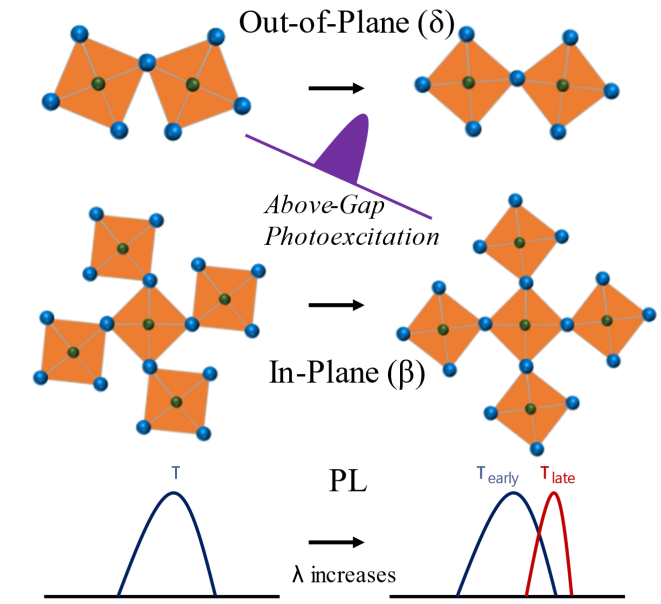
Distorted Pb-I-Pb Angles
Relaxed Pb-I-Pb Angles
Out-of-Plane (δ)
Above-Gap
Photoexcitation
In-Plane (β)
T
PL
T early
T late
λ increases

Advanced Materials https://doi.org/10.1002/adma.202202709

https://onlinelibrary.wiley.com/doi/10.1002/adma.202202709

Supplementary Information

$(BA)_2PbI_4$ and $(PEA)_2PbI_4$ Crystal Synthesis[1]

1 mmol of lead oxide (PbO) was dissolved in 10 mL of hydroiodic acid (HI) under stirring at 150°C. In a separate vial, 2 mmol of butylamine or phenethylamine (depending on the desired perovskite) were protonated with 2 mL of hypophosphorous acid. This solution was added to the hot PbO solution and stirred to complete dissolution. The heating and stirring were then turned off, and the solution was allowed to cool to room temperature. As the solution cooled, orange plates of $(BA)_2PbI_4$ or $(PEA)_2PbI_4$ precipitated out. The resultant crystals were dried via vacuum filtration then placed in a desiccator.

Thin Film Synthesis

To prepare thin films, 200 mg of crystals were dissolved in 1 mL of dimethylformamide and filtered with a 0.45 um PTFE syringe filter. Single crystal sapphire substrates (1 mm by 25.4 mm) were prepared by sonicating for five minutes in washes of soapy water, deionized water, and acetone, then cleaned via UV-ozone exposure for 20 minutes. Thin films were fabricated by spinning the desired precursor solution onto the prepared substrates at 1000 rpm for 10 seconds. These were annealed immediately after spincoating at 50°C for 10 minutes. The annealed perovskite films were coated with a solution of polymethyl methacrylate (PMMA, 300 mg per 5 mL chlorobenzene) to reduce beam damage, then annealed again for 10 minutes at 100°C to cure the polymer.

Single Crystal Synthesis

Suitable crystals for single crystal X-ray diffraction (XRD) were grown to a size of approximately 100x100x50 μm^3 by initially preparing a saturated solution as discussed above. Some solution was then placed in the center of a drop of paratone oil on a glass slide such that the saturated solution to oil ratio was approximately 1:3 by volume. This was allowed to sit and thereby spread out into the oil and crystals were precipitated inside the saturated solution near the oil/acid boundary over the course of about 5 hours. The largest single domain crystal of the above-mentioned size was screened through a polarizing light microscope and then used for single crystal experiments.

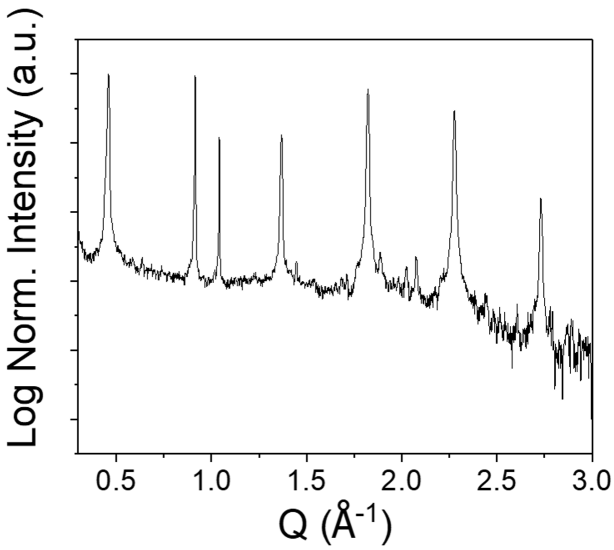

Figure S1: PXRD pattern of $(BA)_2PbI_4$ thin film on a logarithmic scale.

Transient X-ray Diffraction (TrXRD)[2]

Experiment

Experiments were run at Beamline 11-ID-D of the Advanced Photon Source at Argonne National Laboratory. Thin films of 1 μm thickness were mounted at a 4° tilt angle to the incident X-ray source, and were spun at 10,000 rpm during measurement to reduce degradation. The

excitation source of 400 nm was generated from frequency doubling of the 800 nm output from a 1.2 ps Ti:sapphire oscillator operating at 10 kHz. The synchrotron probe consisted of 11.7 keV, 79 ps pulsed X-rays. Diffraction patterns of the thin films were collected on a gated Pilatus 2M detector, then were azimuthally integrated to yield 1D powder X-ray diffraction patterns. A CeO_2 standard was used to calibrate Q prior to data collection. Patterns were collected over 20 cycles of 15 second exposures. Static patterns (pre-excitation) were taken once every five scans to check for possible sample degradation.

TrXRD Data Processing and Statistical Analysis

Area detector plate images were azimuthally integrated to generate 1D powder X-ray diffraction patterns as a function of Q ($Å^{-1}$). These integrated PXRD patterns were normalized to account for changes in synchrotron X-ray flux using the average scattering intensity in a region where there are no Bragg peaks.

For each time delay, a static diffraction pattern taken pre-time-zero (t = -5 ns) was subtracted from the post-photo-excitation pattern (t > 0 ps) to yield transient diffraction patterns following the formula $\Delta S(t) = S(t) - S(0)$. A new static, pre-time-zero pattern was collected every four transient patterns and compared to the first static pattern to account for any changes in sample stability or ambient conditions such as temperature or relative humidity. For each data collection, 4 separate cycles were measured. After each cycle, the sample was translated laterally by a millimeter to account for any degradation that may have occurred.

All transient patterns were smoothed every 5 data points. To produce non-differenced diffraction patterns representative of the photoexcited sample, the static and post-excitation

patterns were added together for each time delay of interest. To account for any "negative" diffraction resulting from this process, the static pattern was multiplied by a constant value.

The lineshapes of the differenced patterns can resemble symmetric derivatives, in which the peaks in the photoexcited material continue to diffract and have only shifted to lower Q, typical of thermal expansion. In addition, the positive lobes of the differential scattering can be larger or smaller than the negative lobes. These shapes indicate that the peaks in the photoexcited material have both shifted to lower Q and either gained or lost diffraction intensity relative to the static peak, suggesting crystallographic ordering or disordering, respectively. Signals that appear as only positive differential signals can relate a new lattice plane relative to the static structure, and are therefore indicative of changes in symmetry. OriginLab and MATLAB were used for all analysis and plotting.

Fitting the Recovery

The time points between 1 ns and 10 us along each plane of interest were fit to the biexponential equation $y = y_o + A_1 e^{-\frac{x}{\tau_1}} + A_2 e^{-\frac{x}{\tau_2}}$. These time points were selected as they represent the recovery in both material systems studied here. The resulting values of τ_1 and τ_2 and errors are reported in Table 1 in nanoseconds; some values for high angle planes are not included due to low signal/noise.

		(002)	**(004)**	**(006)**	**(008)**	**(0 0 10)**
$(BA)_2PbI_4$ 22 μJ/cm^2	τ_1	2.6 ± 0.6	N/A	N/A	N/A	N/A
	τ_2	333 ± 71	N/A	N/A	N/A	N/A
$(BA)_2PbI_4$ 75 μJ/cm^2	τ_1	3.2 ± 0.5	2.3 ± 0.5	2.8 ± 0.5	2.8 ± 0.5	2.6 ± 0.34
	τ_2	436 ± 54	432 ± 57	315±0.42	227±0.37	362 ± 0.5
$(BA)_2PbI_4$ 137 μJ/cm^2	τ_1	1.8 ± 0.6	N/A	N/A	N/A	N/A
	τ_2	481 ± 72	N/A	N/A	N/A	N/A
$(PEA)_2PbI_4$	τ_1	2.7±0.5	2.2 ± 0.5	1.7 ± 0.4	0.87 ± 0.2	N/A

140 μJ/cm^2	τ_2	350 ± 39	424 ± 40	483 ± 42	533 ± 54	N/A

Table 1: TrXRD recovery time constants for $(BA)_2PbI_4$ and $(PEA)_2PbI_4$.

Static Electronic Properties

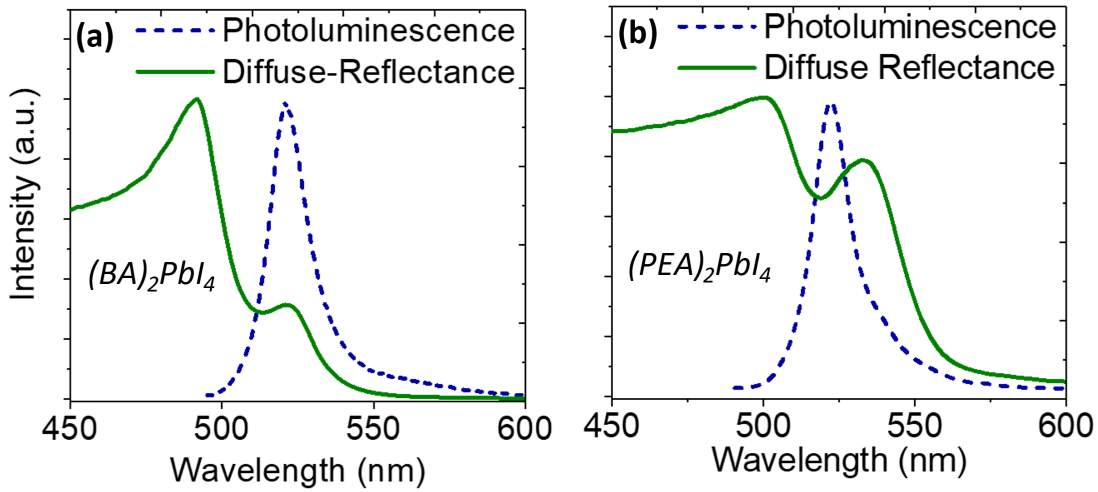

Figure S2: Static photoluminescence and diffuse-reflectance UV-vis of (a) $(BA)_2PbI_4$ and (b) $(PEA)_2PbI_4$ showing emission (dotted blue line) and absorption (solid green line), respectively.

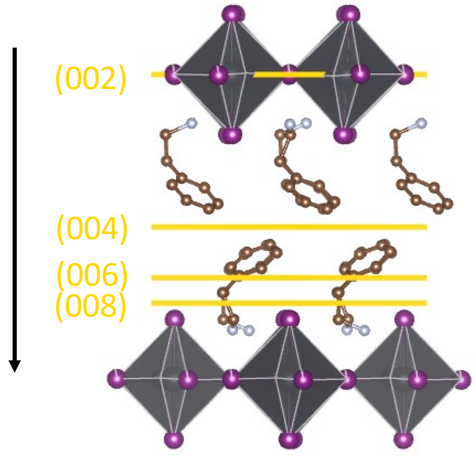

Figure S3: Crystal structure of $(PEA)_2PbI_4$ showing the (002), (004), (006), and (008) planes.

TrXRD Setup

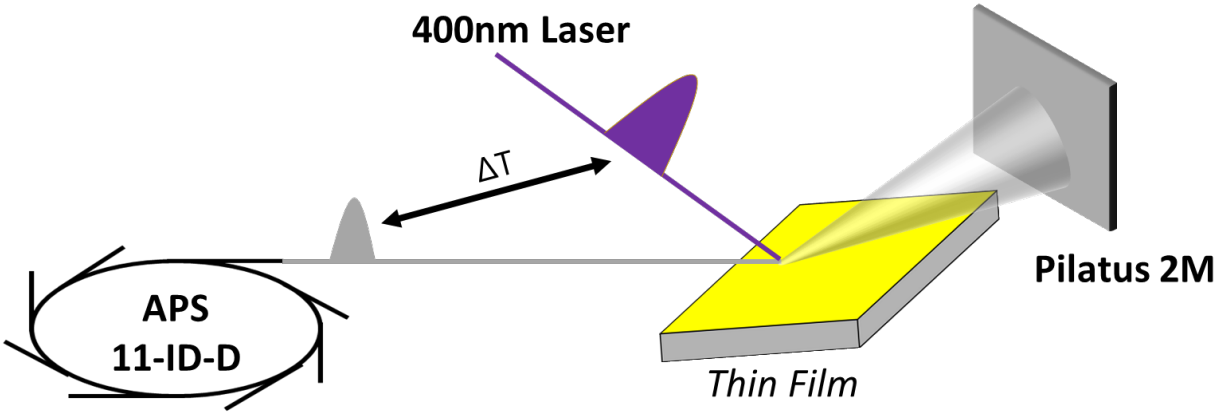

Figure S4: TrXRD setup. Laser pump and synchrotron are spatially overlapped on the surface of the thin film sample, and diffraction is collected by a Pilatus 2M Si detector.

Differential Scanning Calorimetry

Differential scanning calorimetry (DSC) measurements were performed with a TA Q200 instrument. Powder sample was placed in an aluminum crucible that was cold sealed with a press. Sample was measured under ultra-high purity nitrogen gas (50 ml/min) and an empty aluminum was used as a reference. Baseline signal, collected with no crucibles loaded in the cell, was subtracted automatically from the raw data. Temperature was changed at a rate of 2°C/min from -50°C to 150°C.

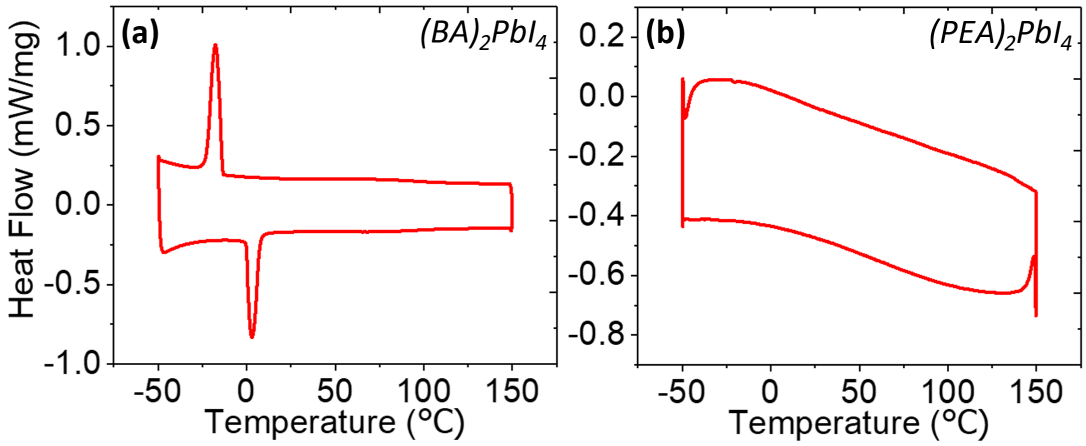

Figure S5: Differential scanning calorimetry heating and cooling curves of (a) $(BA)_2PbI_4$ showing a phase transition at 0°C and (b) $(PEA)_2PbI_4$ showing no phase transition across the temperatures measured.

Supplementary TrXRD and Variable Temperature Powder XRD

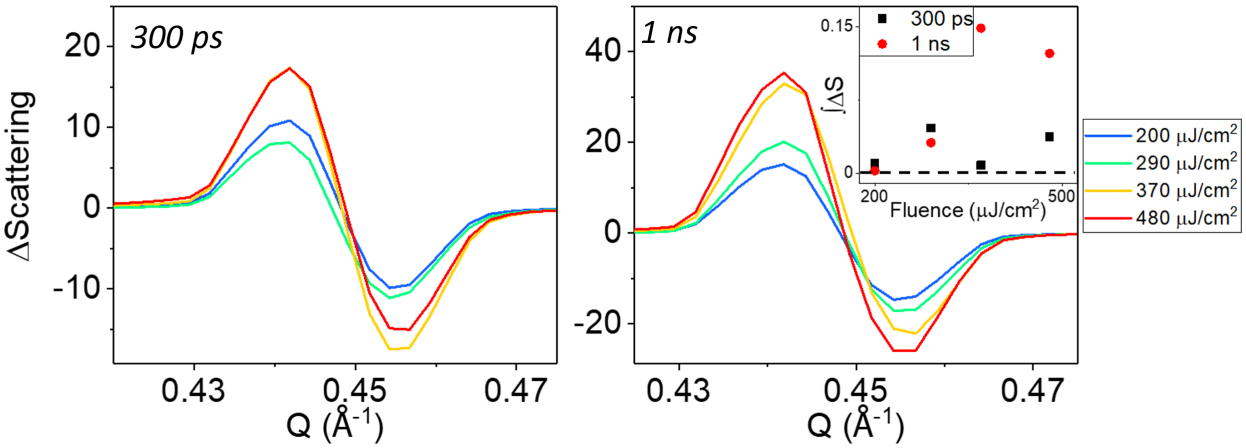

Figure S5: High fluence TrXRD data for $(BA)_2PbI_4$ at 300 ps and 1 ns. Inset is the integrated ΔS curves at the same fluences and time delays.

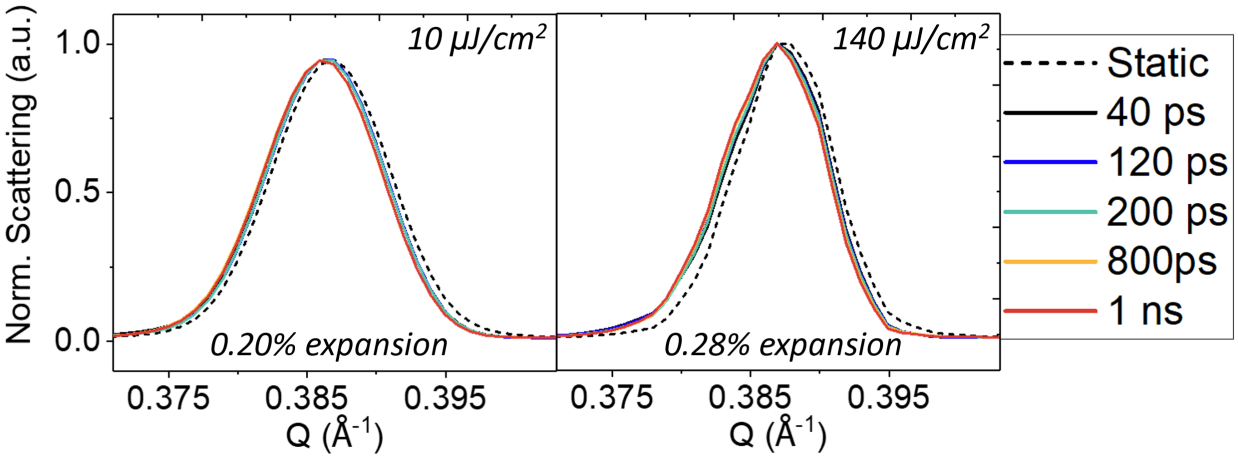

Figure S6: PXRD scans of the (002) plane of $(PEA)_2PbI_4$ normalized to 1 resulting from adding differenced data back to the static PXRD pattern at 10 μJ/cm^2 and 140 μJ/cm^2.

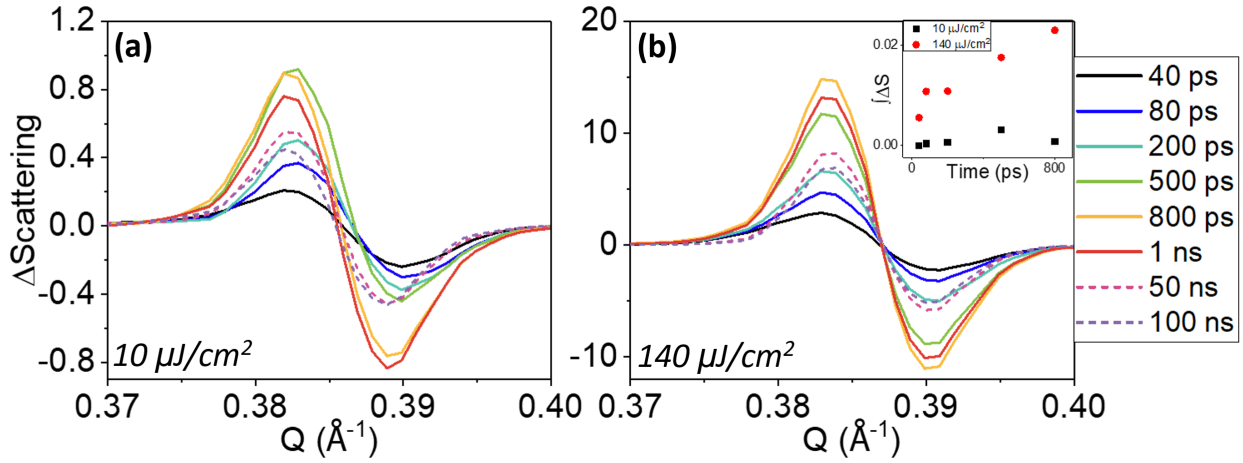

Figure S8: Differential TrXRD patterns of $(PEA)_2PbI_4$ (along the (002) plane at (a) 10.9 μJ/cm^2 and (b) 140 μJ/cm^2 showing increased post-photoexcitation signal at all time delays. Inset is the integrated ΔS curves at the same fluences and time delays.

TrXRD of (00*l*) Reflections (where *l* = 4, 6, 8, 10) for $(PEA)_2PbI_4$ and $(BA)_2PbI_4$

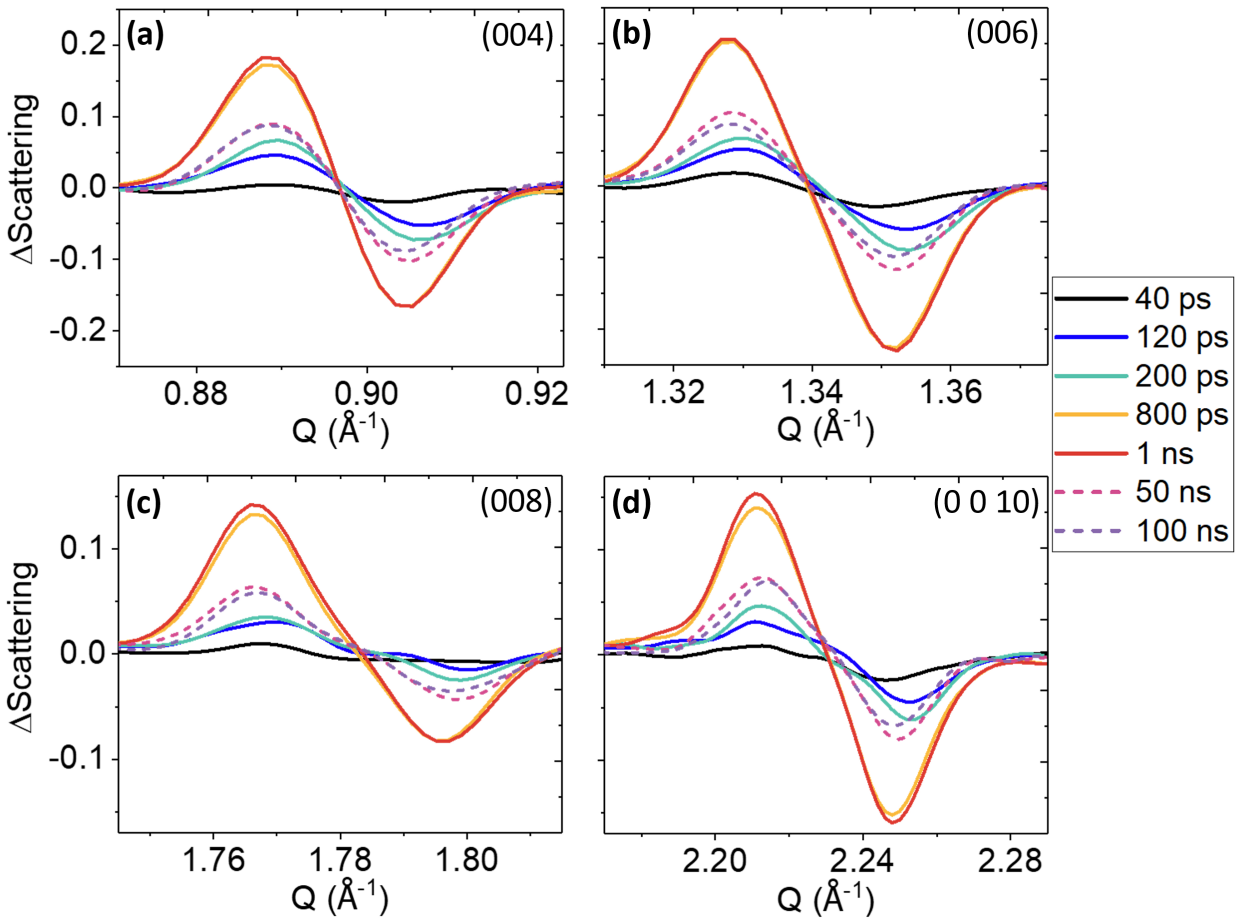

Figure S7: Differential TrXRD patterns of the high angle, in-plane directions of $(BA)_2PbI_4$ at 75 μJ/cm^2. Slight ordering is seen in (a), while thermal expansion is most significant in (b), (c), and (d). Non-symmetric signals in (c) are due to overlap with another peak at higher Q.

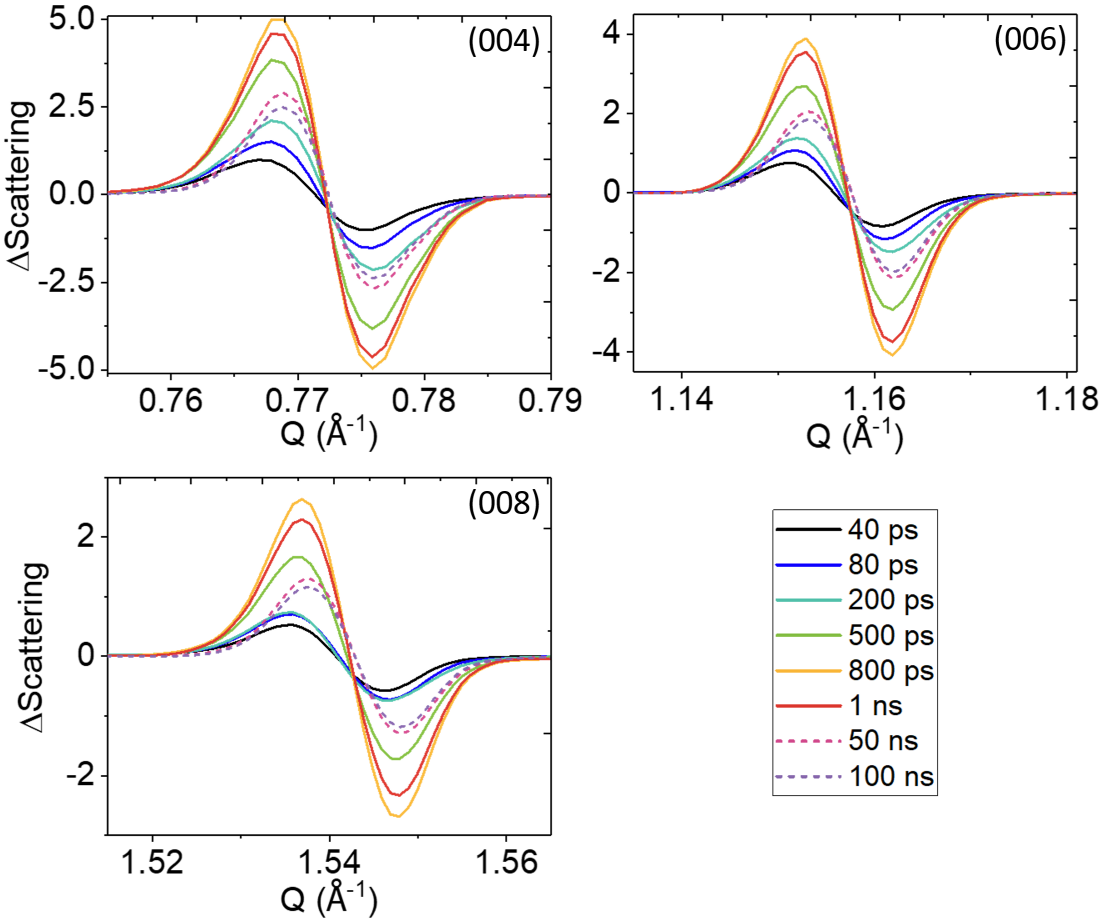

Figure S8: (004), (006), and (008) planes of $(PEA)_2PbI_4$ at 140 uJ/cm^2.

Temperature Changes Upon Photoexcitation

Changes in the temperature of ($BA0_2PbI_4$ and $(PEA)_2PbI_4$ upon photoexcitation were calculated using Q = mCΔT. Values for the absorption coefficients and heat capacities were taken from reference.[3]

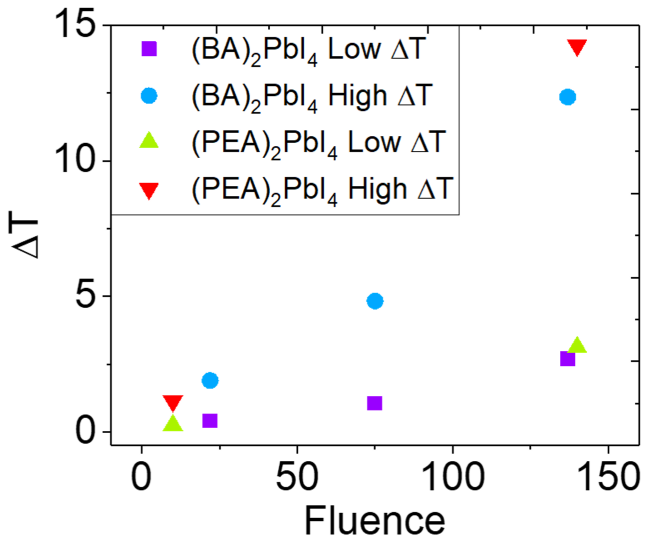

Figure S9: Estimated temperature changes occurring in $(BA)_2PbI_4$ and $(PEA)_2PbI_4$ as a result of pumping with 400 nm.

Variable Temperature Powder X-ray Diffraction

Intensity data of an orange powder were collected at 300-340 K. The powder was mounted in a quartz capillary on a STOE StadiVari diffractometer equipped with an AXO Ag Kα micro-focus sealed Xray A-MiXS source (λ = 0.560834 Å), running at 65 kV and 0.68 mA, and a Dectris Pilatus3 R CdTe 300K Hybrid Photon Counting detector. Temperature of the sample was controlled with an Oxford Cryosystems low temperature device. Data reduction was performed with GSAS.

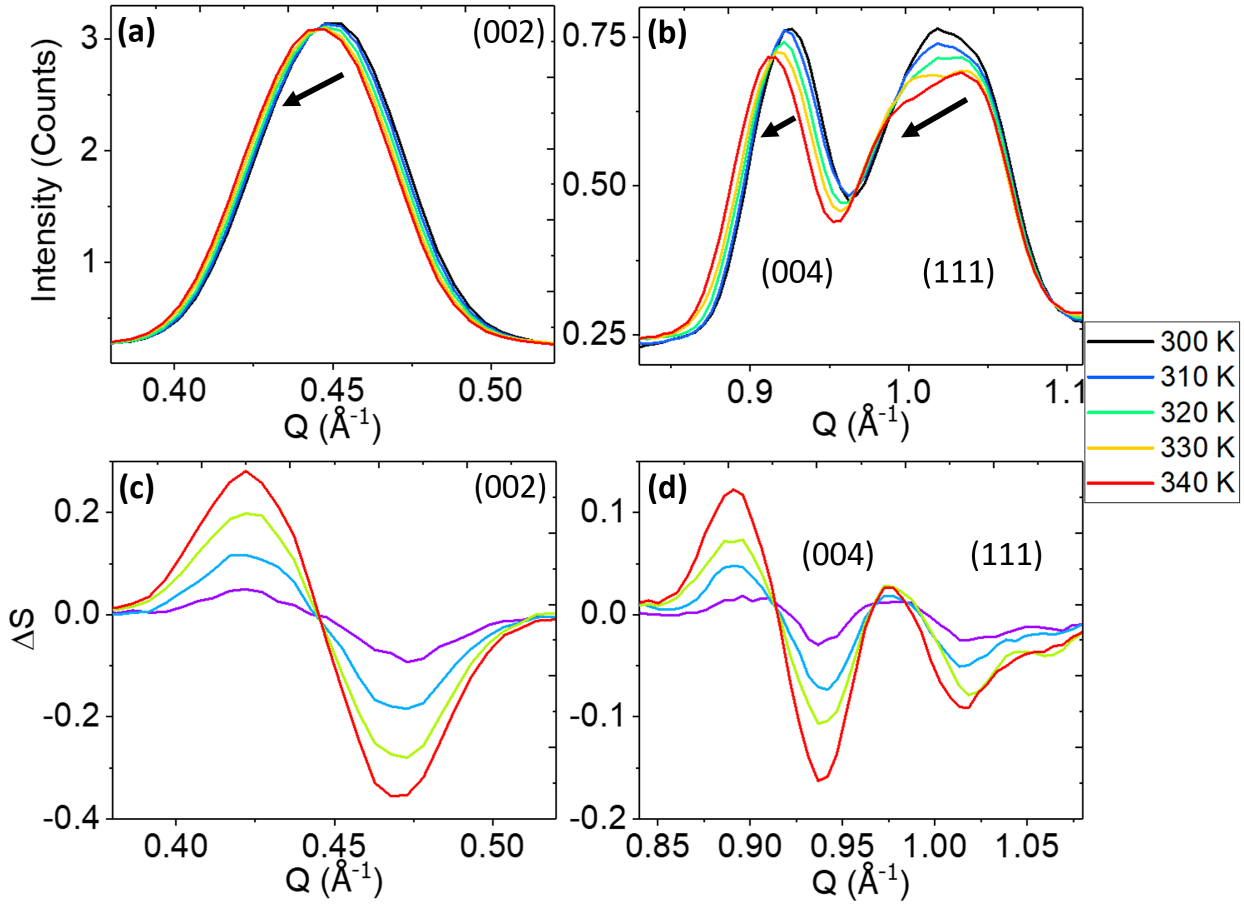

Figure S10: Variable temperature powder XRD patterns of $(BA)_2PbI_4$ at the (002) (a), (004) and (111) (b) reflections. This data has been differenced ((c) and (d)) to more closely observe the peaks shifting and loss of intensity as a result of heating.

Single Crystal X-ray Diffraction

Intensity data was collected from a suitable rectangular platelet shaped single crystal that was mounted on a glass fiber with superglue on a STOE StadiVari diffractometer at 293 K. The diffractometer was equipped with an AXO Auxilia Microfocus Ag Kα (λ = 0.56083 Å) sealed X-ray source and a Dectris Pilatus3 R CdTe 300K Hybrid Photon Counting detector. Data reduction was performed with the STOE X-Area version 1.90 software package with a numerical absorption

correction applied using both STOE X-Red version 1.65.2 and STOE X-Shape version 2.21 and scaling and outlier rejection with STOE LANA version 1.83.8. The structure was solved using the ShelXT intrinsic phasing solution method and was refined with ShelXL full matrix least squares minimization on F^2 method. Olex2 was used as the graphical interface software. The crystallographic information can be found in the supporting information.

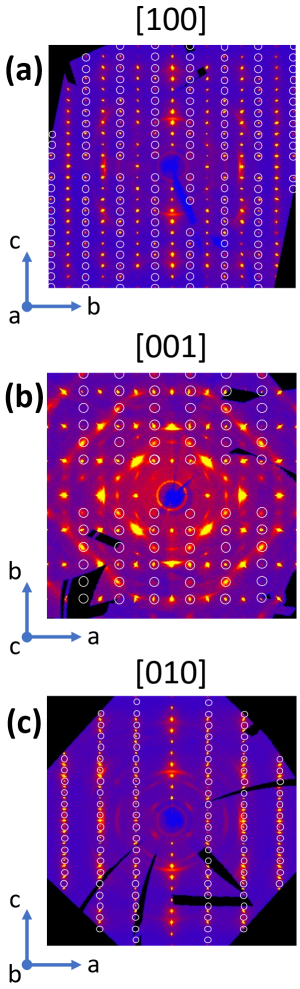

Figure S11: Synthesized precession images from single crystal diffraction data oriented down the (a) [100], (b) [001], and (c) [010] directions. Reflections enclosed in white circles violate the glide plane systematic absence conditions in the *Pbca* space group.

Forbidden Reflections in Pbca

H	K	L	I	σ	I/σ
-2	0	1	102.66	0.38	270.1579
-2	0	-1	105.97	0.44	240.8409
2	0	1	100.02	0.42	238.1429
-2	0	1	102.74	0.44	233.5
-2	0	-7	76.16	0.36	211.5556
-4	0	-11	159.3	0.8	199.125
2	0	-7	74.24	0.39	190.359
-2	0	-7	76.14	0.41	185.7073
4	0	-11	156.57	0.87	179.9655
4	0	11	156.66	0.9	174.0667
2	0	-7	75.72	0.45	168.2667
-2	0	7	75.59	0.45	167.9778
-2	0	-5	36.91	0.24	153.7917
-6	0	-7	92.03	0.63	146.0794
-4	0	-9	96.57	0.68	142.0147
-2	0	-15	80.78	0.59	136.9153
2	0	-15	78.77	0.58	135.8103
-2	0	-3	25.2	0.19	132.6316
4	0	9	96.72	0.73	132.4932
-4	0	9	96.65	0.73	132.3973
2	0	-5	35.68	0.27	132.1481
4	0	-3	71.21	0.54	131.8704
-2	0	-15	78.06	0.61	127.9672
4	0	3	70.19	0.55	127.6182
-4	0	3	68.26	0.54	126.4074
2	0	-15	78.09	0.62	125.9516
-2	0	-5	36.01	0.29	124.1724
2	0	-5	35.83	0.3	119.4333
4	0	-19	53.48	0.48	111.4167
6	0	7	90.26	0.85	106.1882
-2	0	-3	24.33	0.23	105.7826
-6	0	7	89.6	0.85	105.4118
-2	0	-3	24.36	0.25	97.44
-6	0	-15	58.67	0.61	96.18033

-4	0	-1	42.17	0.45	93.71111
-2	0	3	23.55	0.26	90.57692
-4	0	1	42.36	0.47	90.12766
2	0	-13	34.19	0.38	89.97368
2	0	-13	34.23	0.41	83.4878
-4	0	-1	44.12	0.54	81.7037
2	0	-13	33.38	0.41	81.41463
-4	0	1	43.65	0.55	79.36364
4	0	-1	41.67	0.53	78.62264
4	0	1	42.93	0.55	78.05455
-2	0	13	35.02	0.47	74.51064
-6	0	5	42.06	0.57	73.78947
6	0	-5	41.54	0.57	72.87719
6	0	5	42.05	0.58	72.5
-4	0	19	54.33	0.77	70.55844
6	0	15	55.73	0.79	70.5443
-4	0	-13	16.62	0.31	53.6129
-8	0	-3	21.93	0.41	53.4878
-6	0	-13	19.17	0.36	53.25
-6	0	-3	18.74	0.36	52.05556
4	0	-13	15.78	0.31	50.90323
-8	0	-11	29.19	0.59	49.47458
-8	0	-3	23.07	0.47	49.08511
-6	0	-3	20.68	0.46	44.95652
-8	0	-3	22.63	0.51	44.37255
-4	0	13	16.3	0.37	44.05405
6	0	-1	24.47	0.56	43.69643
-6	0	-1	24.73	0.57	43.38596
4	0	-17	16.05	0.37	43.37838
-6	0	-13	19.34	0.45	42.97778
6	0	-3	19.63	0.46	42.67391
-6	0	1	24.12	0.57	42.31579
6	0	3	19.72	0.47	41.95745
4	0	-13	15.83	0.39	40.58974
-8	0	-1	14.14	0.37	38.21622
6	0	13	18.28	0.5	36.56
4	0	-21	14.61	0.45	32.46667
-4	0	-21	13.26	0.43	30.83721
4	0	17	16.89	0.55	30.70909
4	0	-17	16.18	0.53	30.5283

-8	0	-1	13.73	0.45	30.51111
-8	0	1	13.03	0.43	30.30233
8	0	1	13.82	0.46	30.04348
-4	0	17	15.06	0.57	26.42105
2	0	-23	12.86	0.5	25.72
-2	0	-23	9.82	0.39	25.17949
-6	0	-17	15.19	0.61	24.90164
-8	0	-7	7.48	0.32	23.375
-8	0	-19	7.62	0.33	23.09091
6	0	17	12.21	0.54	22.61111
-8	0	-9	7.17	0.35	20.48571
2	0	-17	6.56	0.33	19.87879
6	0	-23	8.45	0.46	18.36957
-8	0	-9	8.04	0.44	18.27273
-2	0	-17	5.23	0.29	18.03448
-8	0	-7	7.35	0.43	17.09302
-4	0	-7	3.68	0.22	16.72727
2	0	-17	5.94	0.36	16.5
-6	0	-11	4.25	0.26	16.34615
-4	0	-7	3.34	0.28	11.92857
-10	0	-7	4.02	0.34	11.82353
-6	0	-9	4.08	0.35	11.65714
-4	0	-5	2.28	0.2	11.4
-10	0	-3	3.96	0.35	11.31429
-4	0	5	2.46	0.22	11.18182
-10	0	3	3.91	0.35	11.17143
6	0	-9	5.37	0.49	10.95918
-10	0	7	3.87	0.36	10.75
2	0	25	4.2	0.4	10.5
4	0	5	2.32	0.23	10.08696
6	0	11	4.26	0.43	9.906977
2	0	-25	3.78	0.39	9.692308
-4	0	-5	2.22	0.23	9.652174
4	0	-7	2.87	0.31	9.258065
-10	0	-1	3.31	0.37	8.945946
-6	0	11	3.86	0.44	8.772727
-10	0	1	3.4	0.39	8.717949
-8	0	-13	3.29	0.38	8.657895
-10	0	-11	2.37	0.29	8.172414
0	0	-9	4.57	0.56	8.160714

4	0	-27	3.99	0.49	8.142857
4	0	-27	3.86	0.49	7.877551
-6	0	9	3.47	0.49	7.081633
2	0	-25	3.7	0.54	6.851852
-10	0	-11	2.09	0.32	6.53125
-10	0	-11	2.43	0.38	6.394737
-8	0	-13	1.77	0.29	6.103448
0	0	5	0.61	0.1	6.1
4	0	7	2.12	0.36	5.888889
6	0	9	2.91	0.51	5.705882
-10	0	-15	1.52	0.27	5.62963
6	0	-25	2.04	0.37	5.513514
1	0	5	0.43	0.08	5.375
0	0	5	0.48	0.09	5.333333
-10	0	-5	2.1	0.4	5.25
-3	0	-1	0.99	0.2	4.95
-3	0	1	0.78	0.16	4.875
3	0	-1	0.92	0.19	4.842105
0	0	-5	0.66	0.14	4.714286
-3	0	1	0.94	0.2	4.7
-8	0	-5	1.14	0.25	4.56
-1	0	-5	0.4	0.09	4.444444
1	0	5	0.31	0.07	4.428571
-10	0	-5	1.4	0.32	4.375
0	0	5	0.51	0.12	4.25
1	0	-5	0.37	0.09	4.111111
-6	0	19	1.33	0.33	4.030303
0	0	-5	0.55	0.14	3.928571
-8	0	-17	1.1	0.29	3.793103
4	0	-29	1.17	0.32	3.65625
-8	0	-5	1.13	0.31	3.645161
0	0	-9	1.62	0.45	3.6
-2	0	-21	0.78	0.22	3.545455
-10	0	-13	1.16	0.33	3.515152
3	0	1	0.64	0.19	3.368421
-8	0	-15	1.17	0.35	3.342857
-8	0	-17	0.96	0.29	3.310345
-3	0	-7	0.4	0.13	3.076923
3	0	-7	0.52	0.17	3.058824
-12	0	13	0.78	0.26	3

0	0	5	0.27	0.09	3
0	0	5	0.3	0.1	3

-10	0	-11	2.09	0.32	6.53125
-10	0	-11	2.43	0.38	6.394737
-8	0	-13	1.77	0.29	6.103448
0	0	5	0.61	0.1	6.1
4	0	7	2.12	0.36	5.888889
6	0	9	2.91	0.51	5.705882
-10	0	-15	1.52	0.27	5.62963
6	0	-25	2.04	0.37	5.513514
1	0	5	0.43	0.08	5.375
0	0	5	0.48	0.09	5.333333
-10	0	-5	2.1	0.4	5.25
-3	0	-1	0.99	0.2	4.95
-3	0	1	0.78	0.16	4.875
3	0	-1	0.92	0.19	4.842105
0	0	-5	0.66	0.14	4.714286
-3	0	1	0.94	0.2	4.7
-8	0	-5	1.14	0.25	4.56
-1	0	-5	0.4	0.09	4.444444
1	0	5	0.31	0.07	4.428571
-10	0	-5	1.4	0.32	4.375
0	0	5	0.51	0.12	4.25
1	0	-5	0.37	0.09	4.111111
-6	0	19	1.33	0.33	4.030303
0	0	-5	0.55	0.14	3.928571
-8	0	-17	1.1	0.29	3.793103

4	0	-29	1.17	0.32	3.65625
-8	0	-5	1.13	0.31	3.645161
0	0	-9	1.62	0.45	3.6
-2	0	-21	0.78	0.22	3.545455
-10	0	-13	1.16	0.33	3.515152
3	0	1	0.64	0.19	3.368421
-8	0	-15	1.17	0.35	3.342857
-8	0	-17	0.96	0.29	3.310345
-3	0	-7	0.4	0.13	3.076923
3	0	-7	0.52	0.17	3.058824
-12	0	13	0.78	0.26	3
0	0	5	0.27	0.09	3
0	0	5	0.3	0.1	3

Table 2: Unmerged hkl reflections violating the *a* glide plane systematic absence condition—(0kl: k = 2n) – in Pbca

H	K	L	I	σ	I/σ
-2	0	1	102.66	0.38	270.1579
-2	0	-1	105.97	0.44	240.8409
2	0	1	100.02	0.42	238.1429
-2	0	1	102.74	0.44	233.5
-2	0	-7	76.16	0.36	211.5556
-4	0	-11	159.3	0.8	199.125
2	0	-7	74.24	0.39	190.359
-2	0	-7	76.14	0.41	185.7073
4	0	-11	156.57	0.87	179.9655
4	0	11	156.66	0.9	174.0667
2	0	-7	75.72	0.45	168.2667
-2	0	7	75.59	0.45	167.9778
-2	0	-5	36.91	0.24	153.7917
-6	0	-7	92.03	0.63	146.0794
-4	0	-9	96.57	0.68	142.0147
-2	0	-15	80.78	0.59	136.9153
2	0	-15	78.77	0.58	135.8103
-2	0	-3	25.2	0.19	132.6316
4	0	9	96.72	0.73	132.4932
-4	0	9	96.65	0.73	132.3973
2	0	-5	35.68	0.27	132.1481
4	0	-3	71.21	0.54	131.8704
-2	0	-15	78.06	0.61	127.9672

4	0	3	70.19	0.55	127.6182
-4	0	3	68.26	0.54	126.4074
2	0	-15	78.09	0.62	125.9516
-2	0	-5	36.01	0.29	124.1724
2	0	-5	35.83	0.3	119.4333
4	0	-19	53.48	0.48	111.4167
6	0	7	90.26	0.85	106.1882
-2	0	-3	24.33	0.23	105.7826
-6	0	7	89.6	0.85	105.4118
-2	0	-3	24.36	0.25	97.44
-6	0	-15	58.67	0.61	96.18033
-4	0	-1	42.17	0.45	93.71111
-2	0	3	23.55	0.26	90.57692
-4	0	1	42.36	0.47	90.12766
2	0	-13	34.19	0.38	89.97368
2	0	-13	34.23	0.41	83.4878
-4	0	-1	44.12	0.54	81.7037
2	0	-13	33.38	0.41	81.41463
-4	0	1	43.65	0.55	79.36364
4	0	-1	41.67	0.53	78.62264
4	0	1	42.93	0.55	78.05455
-2	0	13	35.02	0.47	74.51064
-6	0	5	42.06	0.57	73.78947
6	0	-5	41.54	0.57	72.87719
6	0	5	42.05	0.58	72.5
-4	0	19	54.33	0.77	70.55844
6	0	15	55.73	0.79	70.5443
-4	0	-13	16.62	0.31	53.6129
-8	0	-3	21.93	0.41	53.4878
-6	0	-13	19.17	0.36	53.25
-6	0	-3	18.74	0.36	52.05556
4	0	-13	15.78	0.31	50.90323
-8	0	-11	29.19	0.59	49.47458
-8	0	-3	23.07	0.47	49.08511
-6	0	-3	20.68	0.46	44.95652
-8	0	-3	22.63	0.51	44.37255
-4	0	13	16.3	0.37	44.05405
6	0	-1	24.47	0.56	43.69643
-6	0	-1	24.73	0.57	43.38596
4	0	-17	16.05	0.37	43.37838

-6	0	-13	19.34	0.45	42.97778
6	0	-3	19.63	0.46	42.67391
-6	0	1	24.12	0.57	42.31579
6	0	3	19.72	0.47	41.95745
4	0	-13	15.83	0.39	40.58974
-8	0	-1	14.14	0.37	38.21622
6	0	13	18.28	0.5	36.56
4	0	-21	14.61	0.45	32.46667
-4	0	-21	13.26	0.43	30.83721
4	0	17	16.89	0.55	30.70909
4	0	-17	16.18	0.53	30.5283
-8	0	-1	13.73	0.45	30.51111
-8	0	1	13.03	0.43	30.30233
8	0	1	13.82	0.46	30.04348
-4	0	17	15.06	0.57	26.42105
2	0	-23	12.86	0.5	25.72
-2	0	-23	9.82	0.39	25.17949
-6	0	-17	15.19	0.61	24.90164
-8	0	-7	7.48	0.32	23.375
-8	0	-19	7.62	0.33	23.09091
6	0	17	12.21	0.54	22.61111
-8	0	-9	7.17	0.35	20.48571
2	0	-17	6.56	0.33	19.87879
6	0	-23	8.45	0.46	18.36957
-8	0	-9	8.04	0.44	18.27273
-2	0	-17	5.23	0.29	18.03448
-8	0	-7	7.35	0.43	17.09302
-4	0	-7	3.68	0.22	16.72727
2	0	-17	5.94	0.36	16.5
-6	0	-11	4.25	0.26	16.34615
-4	0	-7	3.34	0.28	11.92857
-10	0	-7	4.02	0.34	11.82353
-6	0	-9	4.08	0.35	11.65714
-4	0	-5	2.28	0.2	11.4
-10	0	-3	3.96	0.35	11.31429
-4	0	5	2.46	0.22	11.18182
-10	0	3	3.91	0.35	11.17143
6	0	-9	5.37	0.49	10.95918
-10	0	7	3.87	0.36	10.75
2	0	25	4.2	0.4	10.5

4	0	5	2.32	0.23	10.08696
6	0	11	4.26	0.43	9.906977
2	0	-25	3.78	0.39	9.692308
-4	0	-5	2.22	0.23	9.652174
4	0	-7	2.87	0.31	9.258065
-10	0	-1	3.31	0.37	8.945946
-6	0	11	3.86	0.44	8.772727
-10	0	1	3.4	0.39	8.717949
-8	0	-13	3.29	0.38	8.657895
-10	0	-11	2.37	0.29	8.172414
0	0	-9	4.57	0.56	8.160714
4	0	-27	3.99	0.49	8.142857
4	0	-27	3.86	0.49	7.877551
-6	0	9	3.47	0.49	7.081633
2	0	-25	3.7	0.54	6.851852
-10	0	-11	2.09	0.32	6.53125
-10	0	-11	2.43	0.38	6.394737
-8	0	-13	1.77	0.29	6.103448
0	0	5	0.61	0.1	6.1
4	0	7	2.12	0.36	5.888889
6	0	9	2.91	0.51	5.705882
-10	0	-15	1.52	0.27	5.62963
6	0	-25	2.04	0.37	5.513514
1	0	5	0.43	0.08	5.375
0	0	5	0.48	0.09	5.333333
-10	0	-5	2.1	0.4	5.25
-3	0	-1	0.99	0.2	4.95
-3	0	1	0.78	0.16	4.875
3	0	-1	0.92	0.19	4.842105
0	0	-5	0.66	0.14	4.714286
-3	0	1	0.94	0.2	4.7
-8	0	-5	1.14	0.25	4.56
-1	0	-5	0.4	0.09	4.444444
1	0	5	0.31	0.07	4.428571
-10	0	-5	1.4	0.32	4.375
0	0	5	0.51	0.12	4.25
1	0	-5	0.37	0.09	4.111111
-6	0	19	1.33	0.33	4.030303
0	0	-5	0.55	0.14	3.928571
-8	0	-17	1.1	0.29	3.793103

4	0	-29	1.17	0.32	3.65625
-8	0	-5	1.13	0.31	3.645161
0	0	-9	1.62	0.45	3.6
-2	0	-21	0.78	0.22	3.545455
-10	0	-13	1.16	0.33	3.515152
3	0	1	0.64	0.19	3.368421
-8	0	-15	1.17	0.35	3.342857
-8	0	-17	0.96	0.29	3.310345
-3	0	-7	0.4	0.13	3.076923
3	0	-7	0.52	0.17	3.058824
-12	0	13	0.78	0.26	3
0	0	5	0.27	0.09	3
0	0	5	0.3	0.1	3

Table 3: Unmerged hkl reflections violating the b glide plane systematic absence condition—(h0l : l = 2n) – in Pbca

H	K	L	I	σ	I/σ
1	4	0	1078.16	1.48	728.4865
-1	-2	0	298.47	0.42	710.6429

-1	-4	0	1093.35	1.76	621.2216
-1	2	0	304.98	0.53	575.434
-1	-4	0	1103.94	2.06	535.8932
-1	-4	0	1097.09	2.08	527.4471
-1	2	0	312.84	0.62	504.5806
-1	6	0	318.31	0.64	497.3594
-1	2	0	311.9	0.65	479.8462
1	2	0	296.66	0.62	478.4839
1	4	0	1087.82	2.29	475.0306
1	-2	0	282.39	0.63	448.2381
-1	2	0	289.88	0.65	445.9692
-1	-2	0	290.55	0.69	421.087
-3	-2	0	317.77	0.78	407.3974
-1	6	0	318.11	0.79	402.6709
-1	-2	0	298.25	0.77	387.3377
-1	6	0	316.02	0.84	376.2143
1	6	0	305.63	0.89	343.4045
-1	6	0	303.48	0.94	322.8511
3	-2	0	314.55	0.99	317.7273
-3	2	0	310.42	0.99	313.5556
1	-6	0	315.51	1.01	312.3861
1	-6	0	310.99	1.3	239.2231
-1	-6	0	298.32	1.35	220.9778
-3	6	0	174.9	0.83	210.7229
3	-6	0	168.09	0.94	178.8191
-7	-4	0	167.04	0.97	172.2062
-7	4	0	182.3	1.09	167.2477
-7	-4	0	179.02	1.25	143.216
-5	2	0	75.23	0.53	141.9434
-5	-2	0	74.17	0.61	121.5902
5	-2	0	75.3	0.67	112.3881
-3	4	0	44.68	0.41	108.9756
-3	4	0	43.44	0.41	105.9512
-1	8	0	38.26	0.37	103.4054
-3	-4	0	43.46	0.46	94.47826
-7	-2	0	36.83	0.39	94.4359
3	-4	0	42.38	0.45	94.17778
-1	8	0	39.32	0.42	93.61905
1	8	0	40.91	0.44	92.97727
1	8	0	40.61	0.44	92.29545

1	8	0	39.2	0.43	91.16279
3	4	0	43.14	0.51	84.58824
-7	2	0	39.05	0.48	81.35417
-9	-2	0	42.92	0.53	80.98113
1	-8	0	39	0.49	79.59184
-3	-8	0	9.5	0.12	79.16667
7	2	0	37.62	0.54	69.66667
-9	-4	0	29.35	0.43	68.25581
-7	2	0	37.73	0.59	63.94915
1	8	0	35.8	0.64	55.9375
-9	-2	0	39.19	0.71	55.19718
-1	-8	0	38.24	0.7	54.62857
-9	4	0	26.93	0.53	50.81132
-5	6	0	16.25	0.33	49.24242
-9	6	0	30.17	0.62	48.66129
-9	4	0	27.68	0.6	46.13333
-5	8	0	15.61	0.34	45.91176
-9	-6	0	29.49	0.72	40.95833
-3	8	0	10.41	0.26	40.03846
-3	8	0	11.58	0.32	36.1875
-5	8	0	15.28	0.44	34.72727
-5	6	0	13.93	0.42	33.16667
-3	8	0	11.51	0.4	28.775
3	-8	0	10.8	0.38	28.42105
-1	0	0	2.12	0.08	26.5
-7	6	0	8.87	0.4	22.175
-3	-8	0	9.76	0.45	21.68889
3	-8	0	10.01	0.47	21.29787
3	8	0	9.82	0.49	20.04082
-7	-6	0	9.35	0.51	18.33333
-7	10	0	4.91	0.32	15.34375
-3	5	0	6.01	0.4	15.025
-11	-4	0	6.45	0.46	14.02174
-3	1	0	2.61	0.19	13.73684
3	-5	0	6.03	0.46	13.1087
-1	12	0	3.53	0.28	12.60714
-5	-3	0	4.37	0.36	12.13889
-1	-3	0	1.5	0.13	11.53846
-1	3	0	1.84	0.16	11.5
-3	1	0	2.82	0.25	11.28

-3	-1	0	2.44	0.22	11.09091
-5	3	0	5.65	0.51	11.07843
-7	1	0	4.17	0.38	10.97368
-5	10	0	2.57	0.24	10.70833
3	-1	0	2.56	0.24	10.66667
-3	5	0	3.6	0.34	10.58824
-7	-10	0	4.6	0.44	10.45455
-1	3	0	1.87	0.18	10.38889
5	3	0	3.7	0.36	10.27778
-11	8	0	3.78	0.37	10.21622
1	-1	0	0.6	0.06	10
1	-3	0	1.79	0.18	9.944444
-1	3	0	1.96	0.2	9.8
-11	6	0	3.14	0.34	9.235294
1	3	0	1.54	0.17	9.058824
-3	-5	0	3.61	0.41	8.804878
-7	-1	0	3.67	0.42	8.738095
1	-12	0	2.62	0.3	8.733333
-1	1	0	0.66	0.08	8.25
-5	-4	0	1.68	0.21	8
-1	-5	0	0.8	0.1	8
-11	-2	0	1.64	0.21	7.809524
-5	10	0	2.33	0.3	7.766667
5	4	0	1.63	0.21	7.761905
-5	1	0	1.7	0.22	7.727273
-1	-3	0	1.57	0.21	7.47619
-1	3	0	1.33	0.18	7.388889
-7	8	0	1.98	0.27	7.333333
7	-1	0	3.58	0.49	7.306122
1	-3	0	1.07	0.15	7.133333
-7	8	0	1.84	0.26	7.076923
1	-3	0	1.13	0.16	7.0625
-1	-1	0	0.49	0.07	7
-5	4	0	1.96	0.29	6.758621
5	4	0	2.02	0.3	6.733333
-11	-8	0	2.84	0.43	6.604651
1	-1	0	0.59	0.09	6.555556
-5	1	0	1.63	0.26	6.269231
1	1	0	0.68	0.11	6.181818
-3	10	0	1.27	0.21	6.047619

-1	-1	0	0.54	0.09	6
5	-1	0	1.72	0.29	5.931034
3	10	0	1.16	0.2	5.8
1	10	0	1.15	0.2	5.75
-1	-5	0	0.85	0.15	5.666667
-3	10	0	1.32	0.24	5.5
-11	2	0	1.87	0.34	5.5
-1	-12	0	2.25	0.41	5.487805
-3	0	0	0.82	0.15	5.466667
3	-10	0	1.35	0.25	5.4
-1	5	0	0.85	0.16	5.3125
-1	10	0	1	0.19	5.263158
-3	10	0	1.12	0.22	5.090909
-1	7	0	0.56	0.11	5.090909
-3	0	0	0.94	0.19	4.947368
-1	5	0	0.68	0.14	4.857143
-1	7	0	1.08	0.24	4.5
-1	5	0	0.45	0.1	4.5
3	5	0	1.97	0.44	4.477273
-5	12	0	1.29	0.29	4.448276
5	1	0	1.07	0.25	4.28
7	5	0	1.59	0.38	4.184211
-3	5	0	1.12	0.27	4.148148
-9	1	0	1.75	0.43	4.069767
-5	-1	0	0.97	0.24	4.041667
-5	7	0	1.93	0.48	4.020833
-5	7	0	1.39	0.35	3.971429
-7	-8	0	1.35	0.34	3.970588
-7	5	0	2.2	0.57	3.859649
-1	7	0	0.8	0.21	3.809524
-7	-5	0	2.49	0.66	3.772727
-7	3	0	1.21	0.33	3.666667
-1	5	0	0.47	0.13	3.615385
-7	12	0	1.15	0.33	3.484848
1	-10	0	1.08	0.31	3.483871
-7	5	0	1.84	0.53	3.471698
-7	-3	0	1.05	0.31	3.387097
-3	9	0	0.57	0.17	3.352941
1	7	0	0.79	0.24	3.291667
-5	-12	0	1.15	0.36	3.194444

-9	-1	0	1.16	0.37	3.135135
1	-5	0	0.5	0.16	3.125
-1	-5	0	0.74	0.24	3.083333

Table 4: Unmerged hkl reflections violating the c glide plane systematic absence condition—(hk0: l = 2n) – in Pbca

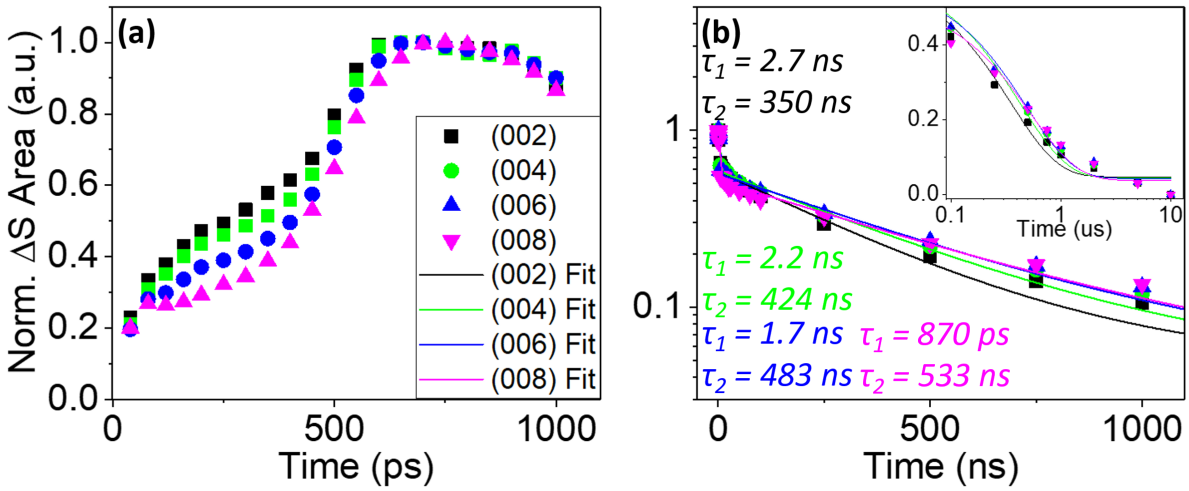

Figure S12: Rise (a) and recovery (b) dynamics of the (002), (004), (006), and (008) planes of $(PEA)_2PbI_4$ at 140 μJ/cm^2 determined by taking the area under the absolute value of the differenced curves at each time delay. Solid lines indicate biexponential fits. The time constants in the recovery do not change significantly between reflection of interest, suggesting that the dynamics of the higher angle planes are dictated by that of the (002).

Time-Resolved Photoluminescence Experiment and Supplementary Data

Time-resolved photoluminescence was measured using a 2 kHz, 35 fs pulse width Ti:sapphire amplifier. Samples were excited using 400 nm pump pulses generated via frequency-doubled 800 nm output produced using a BBO crystal. A single photon-sensitive streak camera with a 0.15m spectrograph was used to measure time-resolved photoluminescence.

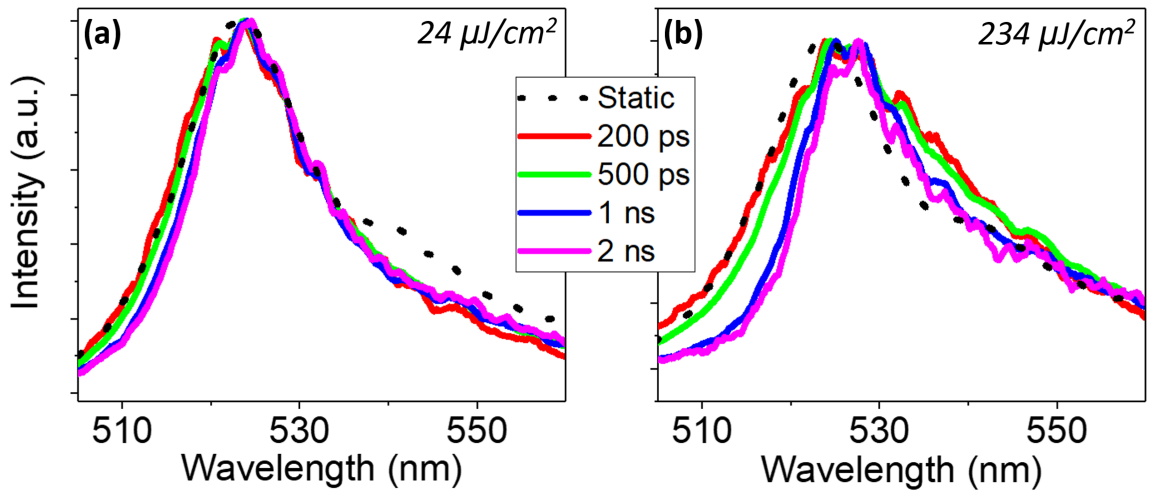

Figure S13: Time-resolved photoluminescence spectra of $(BA)_2PbI_4$ at 24 and 234 μJ/cm^2.

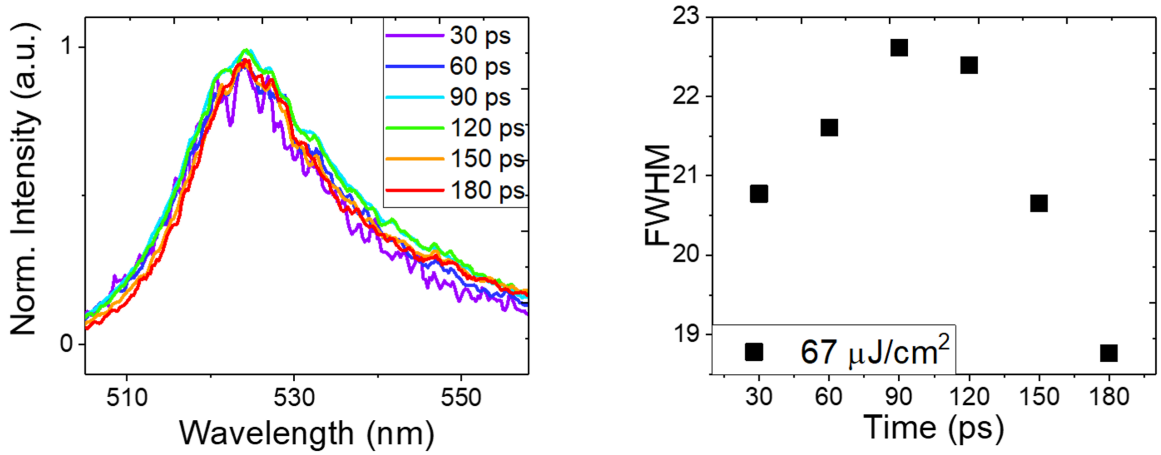

Figure S14: Early time evolution of $(BA)_2PbI_4$ PL at 67 uJ/cm^2.

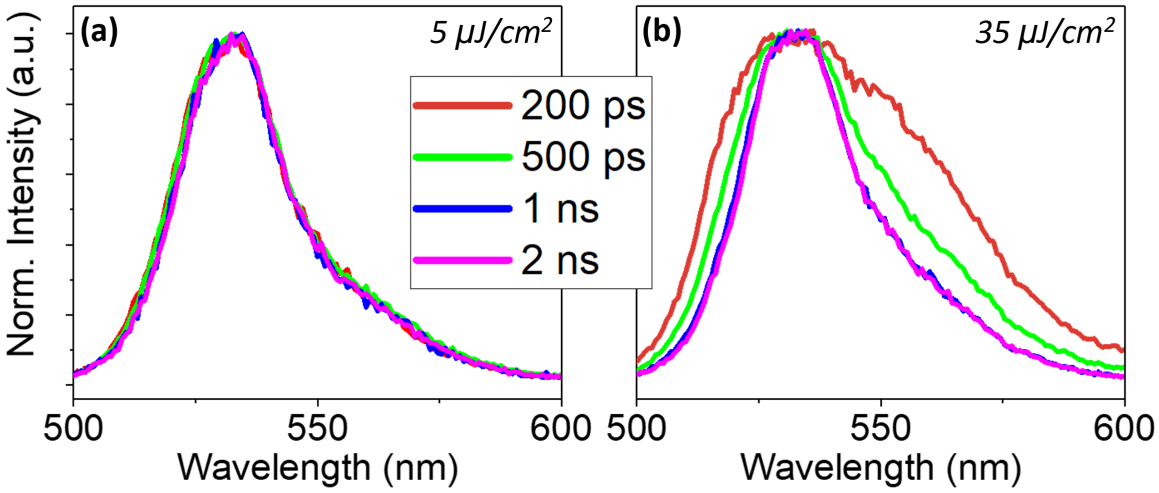

Figure S15: Time-resolved photoluminescence spectra of $(PEA)_2PbI_4$ at low, medium, and high fluences showing narrowing and shifting of the emission similar to observations in $(BA)_2PbI_4$.

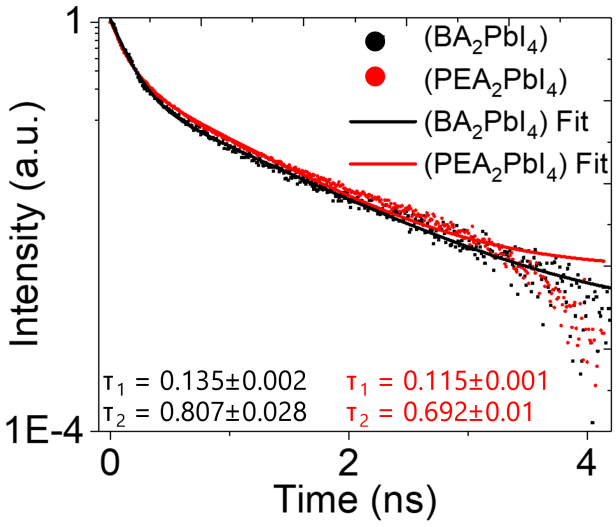

Figure S16: PL lifetimes of $(BA)_2PbI_4$ and $(PEA)_2PbI_4$.

Band Structure Calculations of Pbca, $P2_12_12_1$, and Theoretical Cs_2PbI_4 Model

Computational Details:

The calculations with SIESTA package were performed within the Density Functional Theory (DFT) using a basis set of finite-range of numerical atomic orbitals.[4] We used the Generalized Gradient Approximation (GGA) with Perdew-Burke-Ernzerhof (PBE) functional to describe the exchange-correlation term, and norm-conserving Troullier-Martins pseudopotentials were used for each atomic species to account for the core electrons.[5] $1s^1$, $2s^22p^2$, $2s^22p^3$, $5s^25p^5$, and $6s^26p^25d^{10}$ were used as valence electrons for H, C, N, I and Pb, respectively. Polarized Double-Zeta (DZP) basis set with an energy shift of 200 meV and a Mesh cutoff 400 Rydberg were used for the calculations. The different Brillouin zones were sampled using 6x6x2 k-point grids. Spin-orbit coupling (SOC) was included in its on-site approximation.[6] The bandgaps were corrected using the revisited Slater half-occupation technique in the so-called DFT-1/2 implementation.[7] Hybrid functional (HSE06) calculations were performed using VASP within the Projector Augmented Wave (PAW) formalism.[8] The wave functions were expanded using a plane-wave basis set with an energy cut-off of 400 eV. We used 4x4x1 Γ-centered k-grids to sample the Brillouin zones of the experimental structures. For HSE06, we used α= 0.60 as the amount of the exact exchange. Calculations were performed using either the experimental structures or the Cs_2PbI_4 model structure consisting of rigid octahedra as described in reference 20.[9]

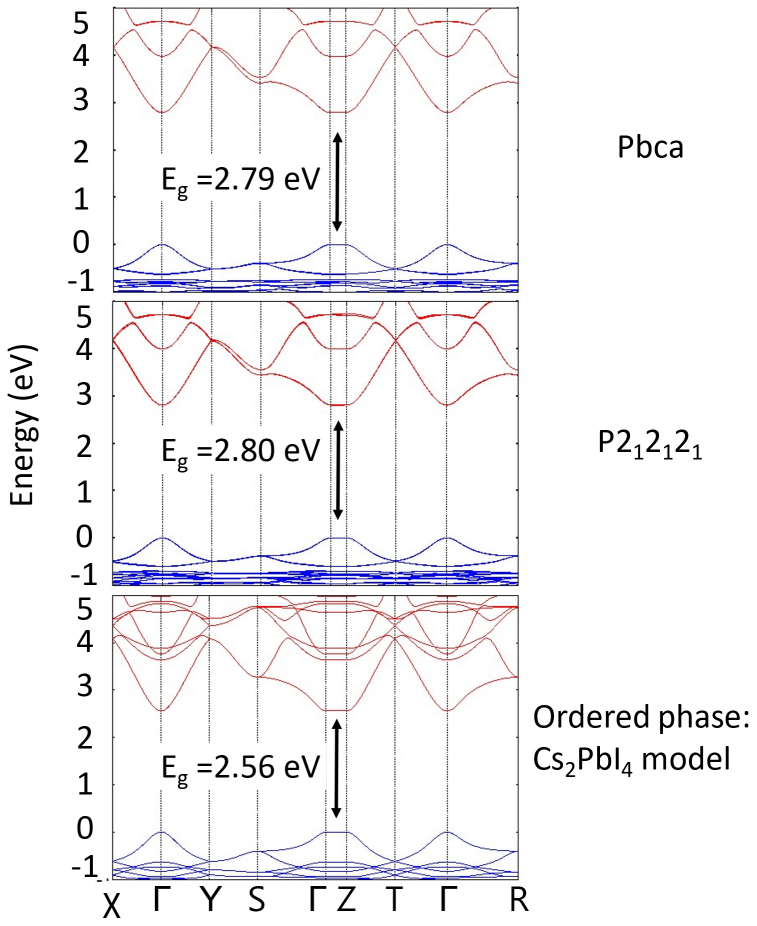

Figure S17: Calculated electronic dispersion curves for the static $P2_12_12_1$ and *Pbca* $(BA)_2PbI_4$ structures and that of a reference structure (Cs_2PbI_4) with all Pb-I-Pb bond angles set to 180°. Upon straightening of these bond angles, the material bandgap redshifts in agreement with time-resolved photoluminescence measurements. The electronic band gaps of the two static structures do not show a significant difference.

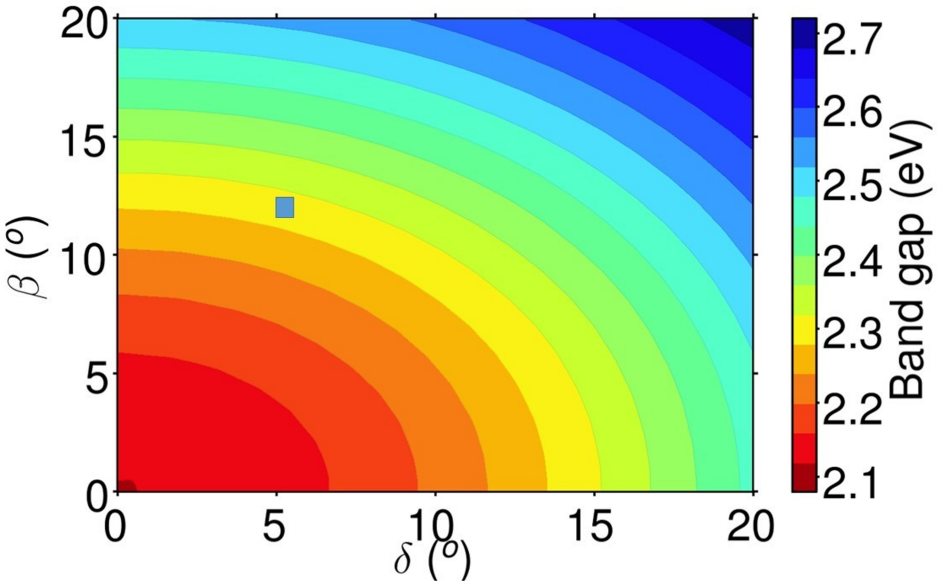

Figure S18: 2D color map of computed electronic bandgap energies of the Cs_2PbI_4 model structure as a function of the out-of-plane δ and in-plane β tilt angles. The calculations are performed at the DFT-1/2 level, including spin-orbit coupling. The average angle derived from the experimental static structure is indicated by a blue square. Note that the predicted bandgap redshift of ~0.2eV between the experimental structure and the one where octahedral tilting is (β=0 and δ=0) is consistent with the one predicted from calculations performed at the HSE06 level (Figure S17).[9]

Crystallographic Tables

Table 1. Crystal data and structure refinement for C8 H24 I4 N2 Pb at 293 K.

Empirical formula	C8 H24 I4 N2 Pb
Formula weight	863.08
Temperature	293 K
Wavelength	0.56086 Å
Crystal system	Orthorhombic
Space group	$P2_12_12_1$
Unit cell dimensions	a = 8.6967(17) Å, α = 90° b = 8.8731(18) Å, β = 90° c = 27.647(6) Å, γ = 90°
Volume	2133.4(7) $Å^3$
Z	4
Density (calculated)	2.687 g/cm^3
Absorption coefficient	7.297 mm^{-1}

F(000)	1520
Crystal size	0.1 x 0.05 x 0.05 mm^3
θ range for data collection	1.902 to 24.999°
Index ranges	-13<=h<=10, -13<=k<=13, -41<=l<=32
Reflections collected	30014
Independent reflections	7631 [R_{int} = 0.0347]
Completeness to θ = 19.665°	100%
Refinement method	Full-matrix least-squares on F^2
Data / restraints / parameters	7631 / 97 / 141
Goodness-of-fit	1.041
Final R indices [I > 2σ(I)]	R_{obs} = 0.0329, wR_{obs} = 0.0792
R indices [all data]	R_{all} = 0.0500, wR_{all} = 0.0889
Extinction coefficient	.
Largest diff. peak and hole	0.789 and -1.230 e·$Å^{-3}$

$R = \Sigma||F_o|-|F_c|| / \Sigma|F_o|$, $wR = \{\Sigma[w(|F_o|^2 - |F_c|^2)^2] / \Sigma[w(|F_o|^4)]\}^{1/2}$ and $w=1/[\sigma^2(Fo^2)+(0.0286P)^2+4.0620P]$ where $P=(Fo^2+2Fc^2)/3$

Table 2. Atomic coordinates ($x10^4$) and equivalent isotropic displacement parameters ($Å^2x10^3$) for C8 H24 I4 N2 Pb at 293 K with estimated standard deviations in parentheses.

Label	x	y	z	Occupancy	U_{eq}*
Pb(1)	7501(1)	7486(1)	2500(1)	1	54(1)
I(4)	9455(1)	4453(1)	2542(1)	1	77(1)
I(2)	5554(1)	10514(1)	2456(1)	1	78(1)
I(3)	7629(2)	7151(2)	1345(1)	1	84(1)
I(1)	7348(2)	7827(2)	3653(1)	1	84(1)
N(1)	6753(19)	3224(14)	1553(5)	1	124(6)
H(1A)	7171.41	4137.04	1574.96	1	149
H(1B)	6590.49	2859.52	1848.54	1	149
H(1C)	5862.7	3285.61	1395.5	1	149
C(1)	7840(30)	2180(20)	1278(8)	1	155(8)
H(1D)	8904.85	2412	1356.15	1	186
H(1E)	7648.86	1133.78	1364.98	1	186
C(2)	7560(30)	2410(20)	756(9)	1	185(11)
H(2A)	7756.48	3440.05	657.53	1	223
H(2B)	6526.59	2118.61	662.96	1	223
C(3)	8900(30)	1200(30)	542(8)	1	172(8)
H(3A)	9940.92	1591.18	549.15	1	207
H(3B)	8840.12	196.47	676.7	1	207
C(4)	8140(40)	1380(40)	87(8)	1	288(19)
H(4A)	8658.43	787.98	-153.38	1	431
H(4B)	8151.22	2419.5	-5.43	1	431
H(4C)	7092.72	1040.12	115.71	1	431
N(2)	8207(10)	11729(11)	3429(4)	1	81(3)
H(2C)	7886.33	11677.81	3123.24	1	97
H(2D)	8065.38	10841.71	3571.77	1	97
H(2E)	9201.27	11964.27	3434.38	1	97
C(6)	7330(30)	12710(30)	4187(8)	1	189(11)
H(6A)	8375.95	12486.64	4283.59	1	227
H(6B)	6732.8	11806.67	4254.84	1	227
C(5)	7350(20)	12860(20)	3679(7)	1	161(9)
H(5A)	7782.23	13833.47	3598.52	1	193
H(5B)	6302.58	12837.52	3561.04	1	193

C(7)	6780(40)	13850(30)	4514(9)	1	249(13)
H(7A)	7689.95	14371.18	4626.14	1	299
H(7B)	6220.25	14559.9	4314.71	1	299
C(8)	5870(30)	13630(30)	4925(7)	1	230(14)
H(8A)	5340.12	14548.67	5001.31	1	345
H(8B)	6511.43	13344.96	5192.43	1	345
H(8C)	5133.24	12846.69	4863.78	1	345

*U_{eq} is defined as one third of the trace of the orthogonalized U_{ij} tensor.

Table 3. Anisotropic displacement parameters ($Å^2x10^3$) for C8 H24 I4 N2 Pb at 293 K with estimated standard deviations in parentheses.

Label	U_{11}	U_{22}	U_{33}	U_{12}	U_{13}	U_{23}
Pb(1)	38(1)	38(1)	85(1)	0(1)	-1(1)	0(1)
I(4)	49(1)	53(1)	130(1)	19(1)	4(1)	10(1)
I(2)	52(1)	53(1)	128(1)	21(1)	11(1)	15(1)
I(3)	85(1)	84(1)	84(1)	2(1)	-4(1)	7(1)
I(1)	84(1)	84(1)	85(1)	-4(1)	-3(1)	10(1)
N(1)	176(15)	91(9)	105(10)	-24(10)	32(10)	-19(9)
C(1)	132(14)	144(14)	188(16)	-38(12)	56(15)	-47(14)
C(2)	180(20)	200(20)	177(16)	-43(17)	29(15)	-80(16)
C(3)	180(20)	181(18)	157(16)	-31(15)	33(14)	-28(15)
C(4)	320(40)	400(40)	143(19)	-10(40)	-4(19)	-70(30)
N(2)	51(5)	81(6)	111(9)	-14(5)	-1(5)	3(6)
C(6)	200(20)	210(20)	153(15)	70(20)	69(15)	5(14)
C(5)	121(15)	196(18)	166(15)	88(15)	44(13)	15(14)
C(7)	320(30)	240(30)	180(20)	60(30)	100(20)	-14(18)
C(8)	250(30)	310(30)	133(19)	70(30)	52(16)	9(18)

The anisotropic displacement factor exponent takes the form: $-2\pi^2[h^2a^{*2}U_{11} + ... + 2hka^*b^*U_{12}]$.

Table 4. Bond lengths [Å] for C8 H24 I4 N2 Pb at 293 K with estimated standard deviations in parentheses.

Label	Distances
Pb(1)-I(4)#1	3.1728(10)
Pb(1)-I(4)	3.1854(10)
Pb(1)-I(2)#2	3.1834(10)
Pb(1)-I(2)	3.1782(10)
Pb(1)-I(3)	3.2092(16)
Pb(1)-I(1)	3.2046(16)
N(1)-H(1A)	0.8900
N(1)-H(1B)	0.8900
N(1)-H(1C)	0.8900
N(1)-C(1)	1.53(2)
C(1)-H(1D)	0.9700
C(1)-H(1E)	0.9700
C(1)-C(2)	1.48(2)
C(2)-H(2A)	0.9700
C(2)-H(2B)	0.9700
C(2)-C(3)	1.69(3)
C(3)-H(3A)	0.9700
C(3)-H(3B)	0.9700
C(3)-C(4)	1.43(2)
C(4)-H(4A)	0.9600
C(4)-H(4B)	0.9600
C(4)-H(4C)	0.9600
N(2)-H(2C)	0.8900
N(2)-H(2D)	0.8900
N(2)-H(2E)	0.8900
N(2)-C(5)	1.424(19)
C(6)-H(6A)	0.9700
C(6)-H(6B)	0.9700
C(6)-C(5)	1.411(19)
C(6)-C(7)	1.44(2)
C(5)-H(5A)	0.9700
C(5)-H(5B)	0.9700

C(7)-H(7A)	0.9700
C(7)-H(7B)	0.9700
C(7)-C(8)	1.40(2)
C(8)-H(8A)	0.9600
C(8)-H(8B)	0.9600
C(8)-H(8C)	0.9600

Symmetry transformations used to generate equivalent atoms:
(1) -x+2,y+1/2,-z+1/2 (2) -x+1,y-1/2,-z+1/2 (3) -x+2,y-1/2,-z+1/2 (4) -x+1,y+1/2,-z+1/2

Table 5. Bond angles [°] for C8 H24 I4 N2 Pb at 293 K with estimated standard deviations in parentheses.

Label	Angles
I(4)#1-Pb(1)-I(4)	91.20(2)
I(4)#1-Pb(1)-I(2)#2	179.93(6)
I(4)#1-Pb(1)-I(2)	88.75(3)
I(4)#1-Pb(1)-I(3)	89.14(4)
I(4)-Pb(1)-I(3)	86.55(3)
I(4)-Pb(1)-I(1)	93.76(4)
I(4)#1-Pb(1)-I(1)	91.13(4)
I(2)-Pb(1)-I(4)	179.86(5)
I(2)#2-Pb(1)-I(4)	88.81(3)
I(2)-Pb(1)-I(2)#2	91.23(2)
I(2)#2-Pb(1)-I(3)	90.94(4)
I(2)-Pb(1)-I(3)	93.33(4)
I(2)-Pb(1)-I(1)	86.37(3)
I(2)#2-Pb(1)-I(1)	88.79(4)
I(1)-Pb(1)-I(3)	179.59(4)
Pb(1)#3-I(4)-Pb(1)	155.29(3)
Pb(1)-I(2)-Pb(1)#4	155.20(3)
H(1A)-N(1)-H(1B)	109.5
H(1A)-N(1)-H(1C)	109.5
H(1B)-N(1)-H(1C)	109.5
C(1)-N(1)-H(1A)	109.5
C(1)-N(1)-H(1B)	109.5
C(1)-N(1)-H(1C)	109.5
N(1)-C(1)-H(1D)	110.3
N(1)-C(1)-H(1E)	110.3
H(1D)-C(1)-H(1E)	108.5
C(2)-C(1)-N(1)	107(2)
C(2)-C(1)-H(1D)	110.3
C(2)-C(1)-H(1E)	110.3
C(1)-C(2)-H(2A)	112.2
C(1)-C(2)-H(2B)	112.2
C(1)-C(2)-C(3)	98(2)

H(2A)-C(2)-H(2B)	109.8
C(3)-C(2)-H(2A)	112.2
C(3)-C(2)-H(2B)	112.2
C(2)-C(3)-H(3A)	114.4
C(2)-C(3)-H(3B)	114.4
H(3A)-C(3)-H(3B)	111.5
C(4)-C(3)-C(2)	86(2)
C(4)-C(3)-H(3A)	114.4
C(4)-C(3)-H(3B)	114.4
C(3)-C(4)-H(4A)	109.5
C(3)-C(4)-H(4B)	109.5
C(3)-C(4)-H(4C)	109.5
H(4A)-C(4)-H(4B)	109.5
H(4A)-C(4)-H(4C)	109.5
H(4B)-C(4)-H(4C)	109.5
H(2C)-N(2)-H(2D)	109.5
H(2C)-N(2)-H(2E)	109.5
H(2D)-N(2)-H(2E)	109.5
C(5)-N(2)-H(2C)	109.5
C(5)-N(2)-H(2D)	109.5
C(5)-N(2)-H(2E)	109.5
H(6A)-C(6)-H(6B)	106.4
C(5)-C(6)-H(6A)	106.2
C(5)-C(6)-H(6B)	106.2
C(5)-C(6)-C(7)	124(2)
C(7)-C(6)-H(6A)	106.2
C(7)-C(6)-H(6B)	106.2
N(2)-C(5)-H(5A)	108.5
N(2)-C(5)-H(5B)	108.5
C(6)-C(5)-N(2)	115.2(17)
C(6)-C(5)-H(5A)	108.5
C(6)-C(5)-H(5B)	108.5
H(5A)-C(5)-H(5B)	107.5
C(6)-C(7)-H(7A)	105.5

C(6)-C(7)-H(7B)	105.5
H(7A)-C(7)-H(7B)	106.1
C(8)-C(7)-C(6)	127(3)
C(8)-C(7)-H(7A)	105.5
C(8)-C(7)-H(7B)	105.5
C(7)-C(8)-H(8A)	109.5
C(7)-C(8)-H(8B)	109.5
C(7)-C(8)-H(8C)	109.5
H(8A)-C(8)-H(8B)	109.5
H(8A)-C(8)-H(8C)	109.5
H(8B)-C(8)-H(8C)	109.5

Symmetry transformations used to generate equivalent atoms:
(1) -x+2,y+1/2,-z+1/2 (2) -x+1,y-1/2,-z+1/2 (3) -x+2,y-1/2,-z+1/2 (4) -x+1,y+1/2,-z+1/2

References

[1] a)D. G. Billing, A. Lemmerer, **2007**, 63, 735; b)K.-z. Du, Q. Tu, X. Zhang, Q. Han, J. Liu, S. Zauscher, D. B. Mitzi, *Inorganic Chemistry* **2017**, 56, 9291.
[2] M. S. Kirschner, D. C. Hannah, B. T. Diroll, X. Zhang, M. J. Wagner, D. Hayes, A. Y. Chang, C. E. Rowland, C. M. Lethiec, G. C. Schatz, L. X. Chen, R. D. Schaller, *Nano Letters* **2017**, 17, 5314.
[3] a)A. Giri, A. Z. Chen, A. Mattoni, K. Aryana, D. Zhang, X. Hu, S.-H. Lee, J. J. Choi, P. E. Hopkins, *Nano Letters* **2020**, 20, 3331; b)B. Song, J. Hou, H. Wang, S. Sidhik, J. Miao, H. Gu, H. Zhang, S. Liu, Z. Fakhraai, J. Even, J.-C. Blancon, A. D. Mohite, D. Jariwala, *ACS Materials Letters* **2021**, 3, 148.
[4] a)J. M. Soler, E. Artacho, J. D. Gale, A. García, J. Junquera, P. Ordejón, D. Sánchez-Portal, *Journal of Physics: Condensed Matter* **2002**, 14, 2745; b)P. Hohenberg, W. Kohn, *Physical Review* **1964**, 136, B864; c)W. Kohn, L. J. Sham, *Physical Review* **1965**, 140, A1133; d)J. Junquera, Ó. Paz, D. Sánchez-Portal, E. Artacho, *Physical Review B* **2001**, 64, 235111.
[5] a)J. P. Perdew, K. Burke, M. Ernzerhof, *Physical Review Letters* **1996**, 77, 3865; b)N. Troullier, J. L. Martins, *Physical Review B* **1991**, 43, 1993.
[6] L. Fernández-Seivane, M. A. Oliveira, S. Sanvito, J. Ferrer, *Journal of Physics: Condensed Matter* **2006**, 18, 7999.
[7] a)L. G. Ferreira, M. Marques, L. K. Teles, *Physical Review B* **2008**, 78, 125116; b)S. X. Tao, X. Cao, P. A. Bobbert, *Scientific Reports* **2017**, 7, 14386.
[8] a)J. Heyd, G. E. Scuseria, M. Ernzerhof, **2003**, 118, 8207; b)G. Kresse, J. Furthmüller, *Physical Review B* **1996**, 54, 11169; c)G. Kresse, J. Furthmüller, *Computational Materials Science* **1996**, 6, 15; d)G. Kresse, D. Joubert, *Physical Review B* **1999**, 59, 1758; e)P. E. Blöchl, *Physical Review B* **1994**, 50, 17953.
[9] L. Pedesseau, D. Sapori, B. Traore, R. Robles, H.-H. Fang, M. A. Loi, H. Tsai, W. Nie, J.-C. Blancon, A. Neukirch, S. Tretiak, A. D. Mohite, C. Katan, J. Even, M. Kepenekian, *ACS Nano* **2016**, 10, 9776.